Word count: 13925

Revision 2

UHP eclogite from western Dabie records evidence of polycyclic burial during continental subduction

Bin Xia*, Yunfeng Shang, Xianbin Lu, Yuanbao Wu

School of Earth Sciences, State Key Laboratory of Geological Processes and Mineral
Resources, China University of Geosciences, Wuhan, China, 430074

*Corresponding author email: xiabin@cug.edu.cn

ABSTRACT

The behavior of continental crust during subduction is important to understand dynamic processes at convergent plate margins. Although simulations have predicted continental crust may experience multiple burial–partial exhumation cycles during subduction, petrological evidence of these cycles is scarce. In this study at Sidaohe, western Dabie, we combine microstructural observations and mineral chemistry with phase equilibrium modeling, conventional Amp–Pl thermobarometry and Zr-in-rutile thermometry to constrain the *P*–*T* evolution for three eclogite samples. All samples have a similar mineral assemblage of garnet + omphacite + symplectite (amphibole + plagioclase ± clinopyroxene) + quartz, with accessory rutile/ilmenite. Element mapping and analytical traverses across large garnets from two samples show obviously systematic variations in Ca and, less strongly, Mg, Fe and X_{Mg} (Mg/(Mg+Fe^{2+})). Based on phase equilibrium modeling and calculated isopleths for grossular, pyrope and X_{Mg} in garnet, we show that *P* first increased from 23.0 to 28.5 kbar, then decreased to 24.0 kbar, before increasing again to a maximum of 30.5 kbar (±1.0 kbar, 2 sigma error) concomitant with a small increase in *T* from 580 to 605 °C (±20 °C, 2 sigma error) at the late prograde stage. These data are interpreted to indicate multiple burial cycles and partial exhumation of eclogite during ongoing continental subduction. After the $P_{\max}$ stage, *T* first increased to a maximum of 664–644 °C at 25.0–20.0 kbar, then decreased to 581–561 °C (±30 °C, 2 sigma error) at 15.0–10.0 kbar based on results of Zr-in-rutile thermometry. Further decompression and cooling occurred across *P*–*T* fields of 590–567 °C at 12.0–10.0 kbar and 520–504 °C (±40 °C, 2 sigma error) at 8.0 kbar. Fine-grained symplectite (clinopyroxene + plagioclase ± amphibole) in the matrix is interpreted to have formed after omphacite due to dehydroxylation of nominally anhydrous minerals during decompression from the $P_{\max}$ stage. By contrast, formation of coarse-grained symplectite (amphibole + plagioclase) and a veinlet of rutile + quartz that crosscuts one sample may be related to influx of externally sourced H_2O. This study shows that (1) evidence of cyclic burial and partial exhumation may be retained in low *T* eclogite during continental subduction, and (2) fluid contributing to widespread retrogression of eclogite during exhumation may be internally and/or externally sourced.

Keywords: eclogite, phase equilibrium modeling, multiple burial cycles, continental subduction, western Dabie

INTRODUCTION

Subduction zones play a key role in deciphering material recycling between Earth's surface and its interior (Zheng et al., 2012). Based on geological and geophysical observations and numerical simulations, a model was developed to understand the dynamics of ocean slab subduction beneath arcs or continents into the mantle (Shreve and Cloos, 1986; Cloos and Shreve, 1988; Gerya et al., 2002). In this model, a subduction channel develops between the upper and lower plates where a mélange of sediments, crustal fragments and fluid accommodates deformation, metamorphism and metasomatism (Shreve and Cloos, 1986). Subsequently, the model was applied to interpret geodynamic processes in continental collision zones (e.g. Zheng et al., 2012; Butler et al., 2013). Similar to the model for oceanic subduction, during continental subduction detached fragments of continental crust were predicted to undergo multiple burial–exhumation cycles due to convective flow (Gerya et al., 2002; Gerya and Stockhert, 2006; Zheng, 2019). However, direct petrological evidence for this behavior is sparse (e.g. Beltrando et al., 2007; Rubatto et al., 2011) and the detailed movements of detached fragments of continental crust during subduction are poorly known.

To understand geodynamic processes operating in continental subduction channels we need robust determination of the *P*–*T* evolution of high-pressure (HP) and ultrahigh-pressure (UHP) rocks (Wei et al., 2010; Li et al., 2016; Xia et al., 2018a; Bovay et al., 2021). Using phase equilibrium modeling and compositional isopleth thermobarometry (Wei et al., 2010; Groppo et al., 2015), we can constrain *P*–*T* conditions from rock-forming minerals in eclogite (e.g. garnet, phengite) under the assumption that the chemical composition was not reset or was only slightly reset during the post-peak metamorphic evolution (Caddick et al., 2010; Rubatto et al., 2011; Bovay et al., 2021). For instance, studies of garnet with growth zonation from eclogite in the Chinese SW Tianshan (Li et al., 2016) and from schists in the Sevier hinterland, USA (Harris et al., 2007) have revealed episodes of sharp increase and decrease in *P*, interpreted to represent multiple burial–exhumation cycles. In both cases, the garnet occurs in rocks with relatively low *T* at the peak stage (<550 °C), which is beneficial for the retention of *P–T* information in compositionally-zoned garnet. However, eclogite in continental subduction zones commonly records higher *T* at the peak or during the retrograde stages (>650 °C; Carswell and Zhang, 1999), which may result in the removal of early-stage *P–T* information due to compositional re-equilibration (Liu et al., 2006; Caddick et al., 2010; Groppo et al., 2015; Xia et al., 2018a).

The Sulu–Dabie belt, which formed during the Triassic collision between the Yangzi and Sino–Korean cratons, has been regarded as the typical example for continental subduction (Fig. 1a; Zheng et al., 2012, 2019). However, no petrological evidence supporting a polycyclic burial–exhumation process has been reported from HP–UHP rocks from the Sulu–Dabie belt. In western Dabie, peak temperature for HP–UHP eclogite was constrained to 520–670 °C at 26.0–31.0 kbar (Zhang and Liou, 1994; Liu et al., 2004, 2006; Wei et al., 2010), distinctly lower than eclogite from the eastern Dabie (average of 700 ± 50 °C at >28.0 kbar) and Sulu (average of 750 ± 50 °C at 29.0–43.0

kbar) belts (Zhang et al., 2009; Suo et al., 2012; Wu and Zheng, 2013; Li et al., 2018; Zheng et al., 2019). In addition, previous studies have shown that garnet from eclogite in western Dabie commonly has growth zoning (Liu et al., 2004, 2006; Wei et al., 2010). Therefore, we infer that early-stage *P–T* information may have been retained in garnet from these eclogites. In this study, we determine *P–T* conditions for the prograde, peak and retrograde stages and construct a complete *P–T* path for eclogite at Sidaohe, western Dabie. Based on phase equilibrium modeling using compositional isopleth thermobarometry, we report changes in *P* from eclogite, which we interpret to represent polycyclic burial–partial exhumation processes during continental subduction.

Mineral abbreviations in this study follow Whitney and Evans (2010).

GEOLOGICAL BACKGROUND

In western Dabie (Fig. 1b; also known as the Hong'an block), various types of metabasite (blueschist, greenschist and eclogite) and serpentinite are mainly enclosed in volumetrically dominant metasedimentary rocks and granitic gneiss as blocks, lenses and occasionally, intercalated layers (Liu et al., 2004). From south to north, based on systematic variations of lithologies and metamorphic grade, six lithotectonic units are subdivided (Fig. 1b; Wei et al., 2010), which are: the Mulanshan greenschist–blueschist unit (peak *P–T* conditions for garnet-bearing blueschist at 5.0–11.0 kbar, 319–427 °C; Liu et al., 2004), the Hong'an HP eclogite unit (peak *P–T* conditions for eclogite at 19.0–26.0 kbar, 485–585 °C; Liu et al., 2004; Lou et al., 2013), the Xinxian UHP eclogite unit ($P_{\max}$ stage *P–T* conditions for eclogite at 28.0–32.0 kbar, 520–670 °C; Zhang and Liou, 1994;

Liu et al., 2004, 2006; Wei et al., 2010), the Huwan HP eclogite unit (peak *P–T* conditions for eclogite at 18.0–23.0 kbar, 540–630 °C; Liu et al., 2004; Ratschbacher et al., 2006), the Balifan mélange unit (*P–T* conditions for a mylonitized quartz–feldspathic schist at 9.0–10.0 kbar, 458–516 °C; Liu et al., 2004) and the Nanwan flysch unit. The variation of metamorphic grade and the architecture of units has been interpreted to represent a huge anticline with UHP rocks at the core and HP rocks at the two limbs, similar to the eastern Dabie belt (Hacker et al., 2000; Liu et al., 2004).

In western Dabie, geochronological studies on eclogite and country rocks have constrained the prograde stage metamorphism to occur at 239–226 Ma, the peak UHP eclogite facies metamorphism at ~226 Ma, the early retrograde eclogite facies metamorphism at 216–213 Ma and the later retrograde amphibolite facies metamorphism at ~212 Ma (Wu and Zheng, 2013 and references therein). These ages are comparable to the eastern Dabie and Sulu belts, indicating they are a huge continuous Triassic orogenic belt. However, in the western segment of the Huwan HP eclogite unit, late Carboniferous ages of ~310 Ma have been reported for eclogite and its country rock gneisses (Wu et al., 2009; Liu et al., 2011). Based on geochemical signatures of some eclogite showing oceanic crust affinity, these ages were interpreted to represent an early oceanic subduction prior to the Triassic continental collision (Wu and Zheng, 2013).

ANALYTICAL METHODS AND SAMPLING

Analytical methods

Initial mineral analyses and element mapping for symplectite were performed using a

JEOL–8230 electron probe microanalyzer with 4 wavelength–dispersive spectrometers (WDS) at the Center for Global Tectonics, School of Earth Sciences, China University of Geosciences (Wuhan). The operating conditions were 15 kV acceleration voltage, 20 nA beam current and 1 μm beam diameter for garnet and clinopyroxene and 5–10 μm beam diameter for amphibole and plagioclase. Raw X-ray intensities were corrected using a ZAF (atomic number, absorption, fluorescence) correction procedure. A series of natural and synthetic SPI standards were used and changed based on the analyzing minerals. The following standards were used: sanidine (K), pyrope garnet (Fe, Al), diopside (Ca, Mg), jadeite (Na), rhodonite (Mn), olivine (Si), rutile (Ti). Elements in unknown samples were all determined within about 2% relative based on analyses of secondary standards. Representative results are given in Tables 1 and 2. Back-scattered Electron (BSE) images and energy dispersive spectrometer (EDS) analyses were obtained using an FEI Quanta 200 scanning electron microscope (SEM) equipped with an EDAX EDS system at the State Key Laboratory of Geological Process and Mineral Resources, China University of Geosciences (Wuhan). The images were obtained at an accelerating voltage of 20 kV with a spot size of 200–400 nm, an emission current of ~100 μA and a working distance of 11–12 mm.

Trace element analyses of rutile grains were performed by the laser ablation-inductively coupled plasma mass spectrometry (LA–ICPMS) method at Wuhan Sample Solution Analytical Technology Co. Ltd. Laser sampling was performed using a GeolasHD laser ablation system (wavelength of 193 nm). Eighty mJ laser energy, 32 μm spot size and 5 Hz laser frequencies were used during the analyses. An Agilent 7900 ICP–MS instrument was used to acquire ion-signal intensities. NIST610, BHVO–2G, BIR–1G and BCR–2G were used as external standards for trace element analysis. Off-line selection and integration of background and analyzed signals, time-drift correction and quantitative calibration for trace element analysis and U–Pb dating were performed by ICPMSDataCal (Liu et al., 2008). For detailed procedure, please reference Liu et al. (2008). For inclusions and matrix rutile, the microbeam analyses were focused on their central part, for megacrystal rutile, two profile analyses were performed. The results are refer to Table 3.

The whole rock compositions were analyzed at the State Key Laboratory of Geological Processes and Mineral Resources, China University of Geosciences (Wuhan) using X-ray fluorescence (XRF) using fused glass disks. The samples were first crushed to less than 60 mesh in a corundum jaw crusher, then to less than 200 mesh in an agate mill. Then, 0.5 g of rock powder, together with 5 g of compound flux ($Li_2B_4O_7$:$LiBO_2$ = 12:22) were fused in a high-frequency melting furnace for 11 minutes at ~1050 °C in 95% Pt–5% Au crucibles. The melt was swirled repeatedly to ensure complete dissolution and homogenization of the material, and then poured into a mold to form a thin flat-surfaced disc (34 mm diameter). The loss-on-ignition (LOI) was measured on dried rock powder by heating in a pre-heated corundum crucible to 1000 °C for 90 minutes and recording the percentage weight loss. XRF analysis was carried out on a Shimadzu XRF–1800 sequential X-ray fluorescence spectrometer, using a Rh-anode X-ray tube with a voltage of 40 kV and current of 70 mA. Calibration curves used for quantification were produced by bivariate regression of data from ~63 reference materials encompassing a wide range of silicate compositions. The measurement procedure and data quality were monitored by repeated samples (one in eight samples), USGS standard AGV–2 and Chinese National standards GSR–1 and GRS–7.

Sampling

In this study, eclogite samples were collected at Sidaohe (115°3′37.33″E, 31°20′32.67″N) in the Xinxian UHP eclogite unit (Fig. 1b). Eclogite occurs as block (4–6 m in diameter) and is enclosed in garnet-bearing felsic gneiss (Fig. 2a). From center to rim, it was more severely retrograded with more abundant quartz veins developed at the edge (Fig. 2a, b).

To qualify *P–T* evolution of the eclogite at Sidaohe, we chose three samples (Sdh–1, Sdh–2 and DB17–06) for detailed petrological analysis. Among which, two (Sdh–1and Sdh–2) were used for phase equilibrium modeling and two (Sdh–1 and DB17–06) for rutile trace element analysis.

PETROLOGY

All samples at Sidaohe, western Dabie show various retrogression in thin sections (Figs. 2c, d; 3). Both eclogite Sdh–1 and Sdh–2 show a granoblastic texture in the scanned thin section (Fig. 2c) and have a similar mineral assemblage of garnet (43–48 vol%) + omphacite (1–3 %) + symplectite of Pl ± Amp ± Cpx (37–42 %) + quartz (10–15 %) and accessory rutile/ilmenite (2–3 %) (Fig. 2c). The eclogite Sdh–1 has slightly more quartz but less symplectite than Sdh–2. For DB17–06 with quartz veinlet, it has been more severely retrogressed with less garnet relics but more Pl ± Amp ± Cpx symplectite in the matrix (Fig. 2d). The veinlet mainly consists of oriented coarse quartz and rutile and Pl ± Amp ± Cpx symplectite (Fig. 2d).

Porphyroblastic garnet (anhedral to subhedral, 0.5–3.0 millimeters in diameter) is cut by fractures filled with dominantly fine-grained amphibole and/or fibrous Amp + Pl ± Rt/Ilm symplectite (Fig. 3a, b, f, h). Coronas of Amp ± Pl develop along garnet rims (Fig. 3h, i). Inclusions in garnet are mainly omphacite, quartz, Pl ± Amp ± Cpx symplectite, with rare epidote, amphibole, rutile/ilmenite and apatite (Fig. 3a–e, k). Traverses of point analyses (Fig. 4a, b) and element mapping (Fig. 4 c–f) across a large porphyroblastic garnet from both Sdh–1 and Sdh–2 show obvious zoning of Ca and, less strongly, Mg, Fe and X_{Mg}, but no Mn from core to rim. For Sdh–1, Grs first decreases from 31 to 25–26 mol% from core to mantle, then increases to 28–29 mol% before decreasing again to 20–21 mol% from mantle to rim. Alm varies antithetically with Grs but consistently with Pyr (Fig. 4a). From core to rim, Alm first slightly increases from 50 to 52 mol%, then decreases to 50 mol% before increasing again to 55 mol%; Prp first increases from 18 to 21–22 mol%, then decreases to 18–20 mol% before increasing again to 23 mol%; X_{Mg} varies from 0.26 to 0.30. For Sdh–2, from core to rim, Grs first decreases from 29 to 24–25 mol%, then increases to 28–29 mol% before decreasing again to 23–24 mol%; Alm first increases from 50 to 52–53 mol%, then decreases to 50 mol% before increasing again to 54 mol%; Prp first increases from 18 to 21–22 mol%, then decreases to 20 mol%

before increasing again to 22 mol%. X_{Mg} varies from 0.25 to 0.29-0.30. Sps varies little from core to rim (1–2 mol%) for both samples (Fig. 4a, b).

Omphacite is only preserved as inclusions in garnet (Fig. 3c, e). In the matrix, it was completely replaced by Pl ± Amp ± Cpx symplectite showing short prismatic or granular shapes (Figs. 2c, 3g, h). The reaction was inferred to be Omp ± H_2O → Pl ± Amp ± Cpx, as has been evidenced by the symplectite partially replacing omphacite in garnet (Fig. 3c). Intergrowths of Cpx, Pl and/or Amp are generally perpendicular to the reaction front (Figs. 3c, g; 5a–g). Previous studies have shown that symplectite usually grew from the original omphacite margins to the reaction front and the thickness of the lamelaes usually decreases with decreasing temperature (Joanny, 1991; Waters, 2003; Lanari et al., 2013). Therefore, in the matrix, we define Cpx-bearing symplectites of Cpx1+ Amp1 + Pl1(mineral grain sizes 50–100 μm in diameter; Figs. 3d, e, g, h, j; 5a, b, d–k) as Sym1 and Cpx2 + Pl2 (commonly <20 μm in diameter; Figs. 3g, h; 5a, b) as Sym2. For the Cpx-absent symplectite of Amp3 + Pl3 (commonly >100 μm; Fig. 3h, i) formed at later amphibolite facies metamorphism (Martin, 2019), we define it as Sym3. For both Sdh–1 and Sdh–2, omphacite included in garnet has constant X_{Jd} of 42–45 mol% while Cpx1 in Sym1 has lower X_{Jd} of 12–26 mol% (Fig. 6a). Composition of Cpx2 in Sym2 was not measured due to its small dimensions (<10 μm in diameter).

Amphibole in eclogite is found in three textural positions: (1) as inclusions in garnet (Fig. 3a, i). For Sdh–1 and Sdh–2, Amp has comparable $^{C}(Al + Fe^{3+} + 2Ti)$ of 1.29–1.93 apfu and $^{A}(Na + K + 2Ca)$ of 0.35–0.70 apfu (23 O basis), mostly ranging from sadanagaite to tschermakite, with only one pargasite (Fig. 6b; Hawthorne et al., 2012); (2) together with Pl constituting Sym1 (Amp1; Fig. 5a, b) and Sym3 (Amp3; Fig. 3g, h, i). For Sdh–1, Amp1 has $^{C}(Al + Fe^{3+} + 2Ti)$ of 0.89–1.41 apfu and $^{A}(Na + K + 2Ca)$ of 0.46–0.58 apfu, ranging from pargasite to magnesiohornblende; Amp3 has $^{C}(Al + Fe^{3+} + 2Ti)$ of 0.79–0.94 apfu and $^{A}(Na + K + 2Ca)$ of 0.15–0.27 apfu, is magnesiohornblende. For Sdh–2, Amp1 has $^{C}(Al + Fe^{3+} + 2Ti)$ of 1.48 apfu and $^{A}(Na + K + 2Ca)$ of 0.50 apfu, is magnesiohornblende; Amp3 has $^{C}(Al + Fe^{3+} + 2Ti)$ of 0.59–1.03 apfu and $^{A}(Na + K + 2Ca)$ of 0.07–0.21 apfu, is magnesiohornblende (Fig. 6b); (3) rimming garnet (Fig. 3i, j) or together with Pl and Rt/Ilm in cracks in garnet (Fig. 3f), has $^{C}(Al + Fe^{3+} + 2Ti)$ of 1.61–1.77 apfu and $^{A}(Na + K + 2Ca)$ of 0.66–0.71 apfu, belonging to Sadanagaite (Fig. 6b).

Plagioclase in both Sym1 and Sym3 is albite with $Ab_{0.92–0.99\ (mean\ 0.96)}$. Epidote is included in garnet but absent in the matrix (Fig. 3a). It has Fe^{3+} of 0.61.

Rutile shows various occurrences in thin sections: as inclusions in garnet (30–100 μm; inclusion Rt as type 1; Fig. 3i); in the matrix (100–300 μm; matrix Rt as type 2; Fig. 3j, k) and as megacrystals in the veinlet (500–4000 μm; megacrystal rutile as type 3; Figs. 2d, 3l). Most of rutile grains have been partially replaced by ilmenite along rims or fractures (Fig. 3j, k, l).

Based on the above petrographic observations and mineral compositions, several stages in the metamorphic evolution of the eclogite at Sidaohe, western Dabie may be inferred. Evidence of the prograde metamorphic stage (M0) is recorded by garnet and its inclusions of omphacite, amphibole, quartz, epidote and rutile (type 1). Pl ± Amp ± Cpx symplectite in the matrix is interpreted to represent former omphacite and is a typical decompression-related texture in eclogite (Joanny, 1991). The peak stage (M1) mineral assemblage is inferred to be Grt + Omp + Qtz + Rt (type 2). The retrograde metamorphic stage (M2) is represented by the breakdown of Omp to form Sym1 (Cpx1+ Amp1 + Pl1) and Sym2 (Cpx2 + Pl2). The late retrograde metamorphic stage (M3) is represented by Sym3 (Amp3 + Pl3) replacing Sym1 and Sym2 (Figure 3e), amphibole/plagioclase and chlorite replacing garnet (Fig. 3c, g). Megacrystal rutile (type 3) in veinlets may be formed prior to stage M3, whereas ilmenite replacing rutile in the matrix may form at this stage.

PHASE EQULIBRIUM MODELLING

To constrain peak *P–T* conditions and metamorphic processes for the eclogite at Sidaohe, western Dabie, phase equilibrium modeling was performed using the THERMOCALC software (version 3.40, updated in March 2014) and the associated internally consistent thermodynamic dataset ds62 (Holland and Powell, 2011; updated in November 2016). The chemical system used for modeling is (Mn)NCFMASHTO ((MnO–)Na_2O–CaO–FeO–MgO–Al_2O_3–SiO_2–H_2O–TiO_2–O) system. A–x relationships used in the modeling are as follows: garnet (White et al., 2014); clinopyroxene and amphibole (Green et al., 2016); plagioclase (Holland and Powell, 2003) and epidote (Holland and Powell, 2011). Rutile, sphene, lawsonite, kyanite, quartz and H_2O are considered to be pure phases.

In the modeling to constrain the prograde to peak *P–T* evolution for the eclogite Sdh–1 and Sdh–2, whole rock compositions obtained by XRF were used after correction of the CaO content for the P_2O_3 contained in apatite (Table 4). O content (equals to Fe_2O_3 in molar percent) was calculated from the whole rock composition of eclogite sampled in the same locality of this study by Yan et al. (2004). In their study using wet chemistry, eclogite and retrograded eclogite gave a consistent Fe_2O_3 (in molar percent)/FeO^T (in molar percent) ratio of 7.5%. H_2O was set to be in excess based on the assumption that the prograde evolution may be H_2O saturated considering the progressive transition from a mineral assemblage dominated by hydrous minerals (e.g. epidote, lawsonite, chlorite and glaucophane) to one dominated by anhydrous minerals (e.g. garnet and omphacite), and the observed abundance of hydrous minerals as inclusions in garnet. To constrain *P–T* conditions for the retrograde stage forming Cpx + Pl + Amp symplectite after omphacite, effective bulk rock composition calculated from equilibrated reaction combined with mineral compositions was used in the phase equilibrium modeling. The balanced reaction forming Sym1 after omphacite using the least square method (software PCalc2.3 by Godard, 2009) applied to compositions of Omp, Cpx1, Pl1 and Amp1 is as follows:

$$1.00\ \mathrm{Omp} + 0.25\ \mathrm{Qtz} + 0.02\ \mathrm{H_2O} = 0.59\ \mathrm{Cpx2} + 0.32\ \mathrm{Pl2} + 0.02\ \mathrm{Amp2} \qquad (1)$$

TiO_2 in the effective bulk composition is same to the value for modeling Figure 7a and H_2O was set to be in excess (Table 4). Sample compositions (in wt%) and corrected or modified bulk compositions (in mol%) used for phase equilibrium modeling are given in

Table 4.

Prograde to peak metamorphic stages

P–T pseudosections constraining the prograde to peak *P–T* evolution for the eclogite Sdh–1 (Fig. 7a) and Sdh–2 (Fig. 7b) were calculated in the MnNCFMASHTO system using the bulk compositions in Table 4 for the *P–T* range 12.0–32.0 kbar and 500–700 °C. Both calculations show similar topology for phase relations. For instance, lawsonite is present in the top-left phase assemblage fields and replaced by epidote at P <21.0 kbar at T <610–615 °C, and by Grt + Omp ± Ky at T >610 °C; glaucophane/hornblende is replaced by Grt + Omp ± Ky at P >20.5 kbar and T >590–595 °C. However, kyanite is modeled to be present at P of 19.5–26.0 kbar at T >610 °C in Fig. 7a, but is absent in Fig. 7b; epidote is modeled to be present across the whole T range in Fig. 7a, but is absent at T >640 °C in Fig. 7b.

Isopleths for Grs (18–38 mol%), Prp (7–26 mol%) and X_{Mg} (0.25–0.30) in garnet and j(o) (Na/(Na+Ca), 0.45–0.54) in omphacite have been calculated for most of the modeled *P–T* range (Fig. 7c, d). The results show that Grs values in garnet roughly decrease while Prp and X_{Mg} values roughly increase with increasing pressure and temperature (Fig. 7c, d). In the phase assemblage fields of Grt + Omp + Lws + Gln + Coe/Qtz + Rt + H_2O, the measured Grs, Prp and X_{Mg} in garnet from Sdh–1 (Grs = 0.31–0.21, Prp = 0.18–0.23 and X_{Mg} = 0.26–0.30) and Sdh–2 (Grs = 0.29–0.23, Prp = 0.18–0.22 and X_{Mg} = 0.25–0.30) define comparable *P–T* fields of 23.0–30.5 kbar, 585–605 °C and 24.5–29.5 kbar, 580–600 °C, respectively (Fig. 7c, d). From garnet core to rim, P first increases from 23.0 to

28.5 kbar, then decreases to 24.0 kbar before increasing again to 30.5 kbar concomitant with a small increase in *T* from 580 to 605 °C (Fig. 7e, g). In the phase assemblage fields of Grt + Omp + Lws ± Gln + Coe/Qtz + Rt + H_2O, isopleths for j(o) of omphacite have steep positive slopes with j(o) values increasing with temperature. In these fields, the measured j(o) of omphacite correspond to *T* ranges of 600–650 °C for Sdh–1 (j(o) = 0.52–0.55) and 595–630 °C for Sdh–2 (j(o) = 0.49–0.51) at 25.0–30.0 kbar, respectively. The inferred peak stage (M1) mineral assemblage characterized by Grt + Omp (represented by Pl ± Amp ± Cpx symplectite) + Coe/Qtz + Rt corresponds to the modeled phase assemblage fields of Grt + Omp + Coe/Qtz + Rt + H_2O, defining temperatures of >640 °C in Fig. 7a and >615 °C in Fig. 7b at *P* >19.5 kbar, respectively. In combination with the *P–T* conditions constrained by isopleths of Grs and Prp in garnet and j(o) of omphacite, a heating process after the P_{max} stage may be inferred (Fig. 7f).

Retrograde metamorphic stage

A *P–T* pseudosection constraining the retrograde *P–T* evolution was calculated for the eclogite Sdh–1 in the NCFMASHTO system using the effective bulk composition in Table 4 for the *P–T* range 5.0–25.0 kbar and 450–650 °C (Fig. 8a). In Fig. 8a, the observed mineral assemblage in Sym1 corresponds to the modeled phase assemblage fields of O/Dio + Hbl + Pl ± Qtz + Rt + H_2O, defining *P* of 5.0–13.0 kbar at the modeled *T* range. In these fields, j(o) values in omphacite increase with increasing pressure and the maximum j(o) content in the symplectitic Cpx2 from Sdh–1 (0.28) and Sdh–2 (0.30) corresponds to pressures of 10.5–11.5 kbar and 11.0–12.0 kbar at 580–650 °C, respectively. The lower j(o) content (0.10–0.27) in omphacite may indicate a decrease of *P* during further exhumation retrogression.

To evaluate H_2O influence on the formation of Sym1, we calculated a P–M_{H2O} pseudosection for the eclogite Sdh–1 in the NCFMASHTO system using the bulk composition in Table 4 at $T = 580$ °C for the *P* range of 5.0–25.0 kbar (Fig. 8b). The H_2O content ranges from 0.00 to 2.00 mol%. In Fig. 8b, free H_2O is present in fields with M_{H2O} above 1.12 mol% and *P* below 21.5 kbar (the red solid line as the H_2O-saturation boundary). The phase assemblage fields of Dio + Hbl + Pl ± Omp ± Qtz ± H_2O develop at *P* below 11.0 kbar and M_{H2O} above 0.56 mol%. Along decompression process during retrogression, eclogite may evolve along the yellow dotted line from A to D with M_{H2O} content of ~1.12 mol% at P <11.0 kbar. We infer H_2O in the bulk rock saturating Sym1 may be ~1.12 mol%, corresponding to 0.4 wt%.

AMP–PL THERMOBAROMETRY

In this study, we use conventional Amp–Pl thermobarometry to constrain *P–T* conditions for the formation of Sym1 with Cpx and Sym3 without Cpx during retrogression. In this study, we calculate temperature for the formation of Sym1 at 12.0 kbar based on the modeling results in Fig. 8a. On the other hand, considering the lower Al_2O_3 content in Amp3 than Amp1 in Sym1 which may yield a *P* difference of ~4.0 kbar using the barometry of Schmidt (1992), we calculate *T* for the formation of Sym3 at 8.0 kbar, similar to that of Martin (2019). The calculation uses the Amp–Pl thermometry B (edenite + albite = richterite + anorthite) by Holland and Blundy (1994). The results show that *T* for Sym1 (calculated at fixed Ab of 0.96) ranges from 567–590 °C and for Sym3 (calculated at fixed Ab of 0.97) ranges from 504–520 °C, respectively. Uncertainties for these results could be ±40 °C within 2 sigma error (Holland and Blundy, 1994).

TRACE ELEMENT COMPOSITION OF RUTILE AND ZR-IN-RUTILE THERMOMETRY

Trace element analyses were applied to rutile with various occurrences from the samples Sdh–1 and DB17–06. Figure 9 shows Nb/Ta vs Nb, Ta and Zr, and Zr vs Sc, U and Hf characteristics for rutile in various occurrences. The inclusion rutile (type 1) has limited variations of Nb/Ta ratios (14.9–17.2) and Nb (322.4–362.6 ppm), Ta (15.5–26.8 ppm), Zr (75–124 ppm) and Hf (2.8–3.7 ppm) contents (Fig. 9a, b, c, f; Table 3). The matrix rutile (type 2) has relatively higher Nb/Ta ratios (15.4–21.0) and Nb (324.3–483.8 ppm), Zr (96–248 ppm) and Hf (3.1–7.1 ppm) contents (Fig. 9a, f) than type 1 rutile. The megacrystal rutile in the veinlets (type 3) has slightly more scattered Nb/Ta ratios (13.9-22.5) and Ta contents (15.5-26.8 ppm; Fig. 9b), but relatively consistent Zr (72–105 ppm), Sc (1.1–2.4 ppm), Hf (3.3–4.5 ppm) and U (0.3–0.9 ppm, except for two analyses 6.1, 4.6 ppm) contents (Fig. 9d, e, f; Table 3).

We use the *P*-dependent Zr-in-rutile thermometry by Tomkins et al. (2007) to calculate temperature for rutile in various occurrences. Beforehand, *P* should be primarily constrained. The inclusion rutile (type 1) armored by garnet has relatively consistent Zr content (Fig. 9c), may imply a closed system to Zr (Zhang et al., 2010). Therefore, we use *P* of 25.0–30.0 kbar at the late prograde stage (Fig. 7f) for further calculation. The Zr content of 75.2–124.3 ppm results in *T* of 608–664 °C with the upper limit of the interquartile *T* range of 634–654 °C (Fig. 10a, c, d). For the matrix rutile (type 2), it has been interpreted to coexist with the main rock-forming minerals (e.g. garnet and omphacite) at $T_{\max}$ or near $T_{\max}$ stages. Therefore, we calculate *T* for type 2 rutile at 25.0–20.0 kbar and the Zr content of 95.7–247.8 ppm resulting in *T* of 698–605 °C with the upper limit of the interquartile *T* range of 664–644 °C (Fig. 10a, c, d). The megacrystal rutile (type 3) in the veinlet may be formed at a later stage at the transition of eclogite to amphibolite facies metamorphism (Zheng et al., 2011a). Therefore, we calculate *T* at 15.0–10.0 kbar and the Zr content of 71.9–105.0 ppm results in *T* of 592–548 °C with the upper limit of the interquartile *T* range of 581–561 °C (Fig. 10b, c, d). The LA–ICPMS analytical error for Zr in rutile is 4.7–16.6 ppm (within 2 sigma), corresponding to *T* uncertainties of 4–6 °C. However, following the recommendation of Tomkins et al. (2007), the uncertainty on *T* could be ~30 °C (within 2 sigma) using Zr-in-rutile thermometry. In this study, we adopt the upper limit of the interquartile *T* range for further discussion as recommended by Taylor–Jones and Powell (2015).

DISCUSSION

P–T evolution

Compositional isopleths including Grs, Prp and X_{Mg} in garnet and j(o) of omphacite in eclogite are commonly used for *P–T* constraint in phase equilibrium modeling (Powell and Holland, 2008; Wei et al., 2010; Groppo et al., 2015; Wang et al., 2020; Xia et al., 2018b, 2020). Although compositional re-equilibration could be expected at *T* >700 °C

(Caddick et al., 2010), modified garnet growth zonation has been identified in MT–UHP eclogite or even in granulite undergoing UHT metamorphic conditions (e.g. O'Brien, 1997; Schmid et al., 2000; Jiao et al., 2021). In this study, because of intense fluid activity during exhumation, the eclogite at Sidaohe in western Dabie have been retrograded during exhumation. However, in carefully selected samples, there are vestiges of prograde information being preserved in large refractory porphyroblastic garnet. We interpret the obvious zoning of Ca in garnet to be original, thus, the fluctuations in Ca contents from core to rim may be due to *P* variations according to our phase equilibrium modeling. On the other hand, the less strong zoning of Mg, Fe and X_{Mg} and no zoning of Mn may be ascribed to partial diffusional re-equilibration during retrogression. The more obvious zoning of Ca than Mg, Fe and Mn in large garnet may be due to its larger ionic size and significantly more sluggish volume diffusion according to numerical modeling (Chakraborty and Ganguly, 1991; Schwandt et al., 1996; Vielzeuf et al., 2007).

When interpreting the results of phase equilibrium modeling, it is important to estimate the uncertainties which may comprise systematic and random uncertainties (Powell and Holland, 2008; Xia et al., 2020). The systematic uncertainties on *P* and *T* propagated from each endmember enthalpy in the dataset are calculated to be ±0.4 kbar and ±12 °C (2 sigma error) using Thermocalc, respectively. On the other hand, the random uncertainties propagated from the analytical uncertainties for EPMA (within ~2% relative) and the AX software for calculating mineral formulae (~1–2% relative) could be ~0.6

kbar on *P* and ~ 10 °C on *T* (2 sigma error; Xia et al., 2020). Therefore, the absolute uncertainties on *P* are ±1.0 kbar and on *T* are ±20 °C (2 sigma error). However, we should take these values as minima if considering other systematic uncertainties propagated from *a*–*x* models and random uncertainties from the bulk rock composition.

By combining the *P*–*T* results from phase equilibrium modeling, Amp–Pl thermobarometry and Zr-in-rutile thermometry, a complete *P*–*T* path is proposed for the eclogite at Sidaohe, western Dabie (Fig. 11), from the prograde stage to the peak stage, and then through several retrograde stages.

The prograde to P_{max} stages. Based on inclusions of Omp + Amp + Ep + Qtz + Rt/Ilm in garnet and the composition of garnet and omphacite, we propose that the prograde *P*–*T* evolution (M0) passed through the modeled phase assemblage fields of Grt + Omp + Lws ± Gln + Coe/Qtz + Rt + H_2O. Lawsonite and glaucophane have not been observed in the thin section, and most likely were replaced by epidote and calcium-rich amphibole (pargasite to tschermakite), respectively, during exhumation (Wei et al., 2010; Lou et al., 2013). Fractures around epidote and amphibole inclusions in garnet (Fig. 3a, b) may have acted as pathways for fluid infiltration to trigger retrogression. Based on garnet compositional isopleth thermobarometry, we propose an increase of *P* from 23.0 to 28.5 kbar, then a decrease to 24.0 kbar, before an increase to 30.5 kbar (± 1.0 kbar, 2 sigma error) concomitant with a small increase in *T* from 580 to 605 °C (±20 °C, 2 sigma error; Fig7. c, d, e). However, since we are uncertain about the extent to which the Prp and X_{Mg} zoning profiles in garnet have been flattened, the *T* results based on Prp and X_{Mg} isopleths in garnet should be treated with appropriate caution. Anyway, we infer two periods of compression separated by a period of decompression during the prograde evolution of the eclogite at Sidaohe, western Dabie (Fig. 7e, f). A compression path with a steep positive slope that reached P–T conditions for the P_{max} stage of 29.0–30.5 kbar/590–605 °C are consistent with the results from an eclogite at Sibian about 20 km to the northwest in the same Xinxian UHP unit (Fig. 1b; Wei et al., 2010). This type of prograde evolution is similar to that modeled for oceanic crust in modern subduction zones due to coupling between the subducting slab and the overlying mantle wedge (e.g., model W1300; Syracuse et al., 2010), but at lower T and has been interpreted to represent fast subduction (Wei et al., 2010). The UHP metamorphism for the P_{max} stage is consistent with the report of coesite pseudomorphs in eclogite at Sidaohe (Yan et al., 2005) and coesite in eclogite and the country rock gneisses in the Xinxian UHP unit (e.g. at Guojiahe and Chengmagang, Fig. 1; Zhang and Liou, 1994; Liu et al., 2004, 2006). In the modeled phase assemblage field of Grt + Omp + Lws + Coe/Qtz + Rt + H_2O (Fig. 7d), a T of 595–650 °C (±20 °C, 2 sigma error) at 25.0–30.0 kbar is constrained by isopleths of j(o) of omphacite and is comparable to the T range of 634–654 °C (±30 °C, 2 sigma error; here and subsequently, we use the upper limit of the interquartile range in T for the Zr-in-rutile thermometry results) recorded by rutile included in garnet (type 1), indicating a T increase after the P_{max} stage (Fig. 10c).

The T_{max} stage. Initial exhumation to the T_{max} stage (M1) produced an inferred mineral assemblage of Grt + Omp + Coe/Qtz + Rt, which indicates the P–T evolution passed through the modeled phase assemblage fields of Grt + Omp + Coe/Qtz + Rt + H_2O after the P_{max} stage (Fig. 7a, b). In these fields, the calculated modal contents of Grt and Omp are 47.0 and 36.7%, respectively, typical of a bimineralic eclogite as observed in thin sections (Fig. 2c). For type 2 rutile in the matrix, using Zr-in-rutile thermometry we have calculated T of 664–644 °C (±30 °C, 2 sigma error) at 25.0–20.0 kbar, interpreted to represent P–T conditions for the T_{max} stage (Fig. 10c, d), similar to the results obtained using conventional thermobarometry by previous researchers (Zhang and Liou, 1994; Liu et al., 2004). Along the P–T path from the P_{max} to T_{max} stages, Gln and Lws disappear via the reactions Lws + Omp + Gln = Grt + Qtz + H_2O and Lws + Omp ± Gln = Grt + Qtz + H_2O, respectively (Figs. 7f, 12).

The retrograde stages. During subsequent exhumation, rock-forming omphacite in the matrix broke down to form Amp + Pl + Cpx symplectite (Sym1). Based on phase equilibrium modeling and conventional Amp–Pl thermometry, we estimate that Sym1 formed at 567–590 °C/12.0 kbar. This T range is similar to the T of 581–561 °C calculated at 15.0–10.0 kbar for type 3 rutile in the veinlets (Fig. 11). These P–T estimates are interpreted to represent a decrease of T during the retrograde stage M2 decompression. Late retrogression (M3) led to the formation of Sym3 at T of 504–520 °C calculated at 8.0 kbar using Amp–Pl thermometry.

Summary. For eclogite at Sidaohe, western Dabie, we propose a P–T path with a prograde segment showing two cycles of P increase to the P_{max} stage, then a T increase during initial exhumation to the T_{max} stage, before a decrease in both P and T during subsequent retrograde stages. The clockwise, open convex *P–T* path is similar to those in the studies of Zhang and Liou (1994) and Liu et al. (2004, 2006) on eclogite from western Dabie, but differs from those in the studies of Wei et al. (2010) and Cheng and Cao (2015) who inferred isothermal decompression after the P_{max} stage.

H_2O behavior along the *P–T* evolution

From the prograde to the P_{max} stage. H_2O contents in the bulk rock are mainly controlled by the stability of hydrous minerals and the *P–T* fields related to various continuous and discontinuous reactions rock crossed during subduction (Schmidt and Poli, 2014; Zheng and Chen, 2016). In this study, *P–T* fields at 23.0–31.0 kbar (with Qz then Coe), 580–600 ℃ were constrained for a segment of the *P–T* evolution from the late prograde to P_{max} stages (Fig. 7f). In these fields, previous experimental studies on metabasite compositions suggest that the hydrous minerals are mainly Lws, Ctd, Ph and Ep/Zoi with Gln decomposed at $P > 23.0$ kbar (Schmidt and Poli, 2014), while Wei et al. (2020) considered the stable minerals to be Lws, Ph, Amp and Ta. In our study, due to the absence of significant K_2O and the low MgO content in the bulk composition (Table 3), Ph and Ta were not formed and H_2O in the bulk rock was retained only in Lws and Gln. Along the *P–T* path from A to B in Fig. 7f, calculated modals of Gln decrease from 12.5 (A) to 0.3 (B) mode% whereas Lws slightly increase from 7.2 to 8.3 mode%. Accordingly, calculated H_2O content in the bulk rock slightly decreases from 0.92 to 0.88 wt%, implying the release of H_2O by the Gln-out reaction is compensated by an increase in modal Lws. Therefore, in subduction zones at low thermal gradients (5–7 ℃/Km), Lws in eclogites could be the most important H_2O reservoir. Indeed, it may take H_2O to 40.0 kbar at T <700 °C, before destabilizing to form normally anhydrous garnet and omphacite (Schmidt and Poli, 2014; Zheng and Chen, 2016; Wei et al., 2020). In addition, numerous studies in Sulu–Dabie and elsewhere have shown that at UHP conditions, nominally anhydrous minerals (NAMs) such as Grt and Omp can incorporate a considerable amount of structural hydroxyl (OH–) and molecular water (H_2O) in point defects within the crystal lattice (Chen et al., 2007), allowing fluid to be carried into the deeper mantle (>200 km), and even to the mantle transition zone (Katayama and Nakasima, 2003; Zheng, 2009).

From the P_{max} to T_{max} stages. In Fig. 7f, the P–T evolution from B to C sequentially crosses the Gln- and Lws-out curves and the modelled H_2O content for relevant assemblages rapidly decreases from 0.88 to 0 wt% (in the modelled assemblages there is no structural hydroxyl in the NAMs). Without considering hydroxyl/H_2O contained in NAMs, the eclogite would become bimineralic and be effectively dry, consistent with our observations (Fig. 2c). The released H_2O may migrate out of the local rock system to promote crust–mantle interactions, the exhumation of deeply subducted continental crust and the retrogression of HP/UHP rocks in continental subduction channels (Chen et al., 2007; Zheng and Chen, 2016).

The retrograde stage. Strong fluid activity during the retrograde exhumation is evidenced by pervasive retrogression and the development of quartz veins/veinlets (Fig. 2c, d). During this process, H_2O may act as a kinetic facilitator for the destabilization of omphacite, as a component of the reaction to form amphibole in symplectite or as a carrier for components required to precipitate minerals in veinlets (Joanny, 1991; Martin, 2019). For UHP eclogite, numerous studies have shown that H_2O may be released from the NAMs during retrograde exhumation (e.g. Chen et al., 2007; Zheng et al., 2011a;). In Sulu–Dabie, the amount of structural hydroxyl could be 115–1300 ppm in omphacite and 92–1735 ppm in garnet (Xia et al., 2005; Chen et al., 2007). The total H_2O concentration including fluid inclusions, hydrous mineral inclusions and structural hydroxyl could even be up to 1170–20745 ppm in Omp and 522–1584 ppm in garnet (Chen et al., 2007).

In this study, Sym2 at the reaction front with only rare or no Amp (Fig. 5c–k) may require very little H_2O for its formation. By contrast, our modeling shows that Sym1, which has Amp several tens of μm in diameter (Fig. 5d–g), requires a H_2O content of 0.4 wt% (equals to 4000 ppm) to hydrate the mineral assemblage (Fig. 8b). Considering Sym1 only developed at limited places around Sym2 (assumed <10 vol% in thin sections; Figs. 2c, 3g), we assume a maximum H_2O content of 400 ppm in the bulk rock may be sufficient to the formation of Sym1. Such an amount of H_2O may be provided by H_2O released from the NAMs during decompression. Therefore, we interpret that the H_2O to trigger the formation of both Sym1 and Sym2 was internally sourced. A similar conclusion was reached by Anderson and Moecher (2007) and Martin (2019) in their studies of symplectite. In support of this interpretation in our study, rutile in the matrix (type 2) has comparable Ta, Sc and U contents to rutile included in garnet (type 1; Fig. 9b, d, e), implying the properties of fluid at this stage had an affinity with that forming type 1 rutile. The high Zr and Hf contents of the matrix rutile may be related to the breakdown of garnet.

The coarse-grained rutile (type 3) in veinlets has more scattered Nb/Ta ratios and Ta contents, but limited variation in Nb, Zr and Hf contents, distinctly different from the inclusion rutile and the matrix rutile (Fig. 9a, b, f), which may imply different properties for the metamorphic fluid compared with that at the prograde to peak stages (Zheng et al., 2011a). We interpret the rutile in veinlets to be formed from an external fluid source with constant Nb, Zr and Hf contents but varied Ta content and Nb/Ta ratios. More abundant quartz veins developed at the transition zone of the eclogite block and the country rock gneisses may support this conclusion (Fig. 2a). The shear zone between the main interface of the eclogitic block and the country rock may act as a preferential path for fluid entering the rock during retrogression (cf. Martin, 2019). Fluid may also promote the formation of Sym3 with coarse-grained Amp and Pl of comparable amount in the matrix, as has been evidenced by its more abundant development near the veinlets (Fig. 2b, d).

IMPLICATIONS

Polycyclic burial of eclogite in continental subduction channel

In this study, our modeling results show that eclogite within a single unit at Sidaohe records two cycles of *P* increase during the prograde metamorphic stage. The first cycle records a *P* increase from 23.0 to 28.5 kbar, followed by partial exhumation and then a second cycle records a *P* increase from 24.0 to 30.5 kbar (Fig. 7e, f). Variations of the minimum to maximum *P* conditions for each cycle are up to 6.5 kbar, implying the two cycles of prograde *P* increase are a reliable result. The result is distinctly different from a single *P–T* loop commonly described for eclogite in Sulu–Dabie by previous studies (Zhang and Liou, 1994; Liu et al., 2004; Cheng and Cao, 2015; Wei et al., 2010; Xia et al., 2018a; Zheng et al., 2019).

In other places in the world, rocks showing *P* cycles during a single orogenic event have been reported and interpreted to represent burial–partial exhumation cycles (Brueckner et al., 2006; Beltrando et al., 2007; Blanco–Quintero et al., 2011; Rubatto et al., 2011; Li et al., 2016). Overall, two scenarios have been proposed to interpret these cycles: (1) they are related to orogenic-scale shortening–extension switches mostly developed in the continental subduction environment (Brueckner et al., 2006; Rubatto et al., 2011), and (2) they are developed within Franciscan-type subduction channels in oceanic subduction zones (Blanco–Quintero et al., 2011; Gerya et al., 2002; Li et al., 2016). In the first case, rocks showing short-term, multiple eclogite facies metamorphism from the Sesia zone in the Italian Western Alps were interpreted to be formed due to oblique subduction along the convergent plate margin. Episodic switches from transpressional to transtensional deformation led to alternating burial and partial exhumation for rocks in the subduction zone (Rubatto et al., 2011). In the second case, convective movement of rocks occurs within a thin and rapidly sheared layer of unconsolidated sediments (Lister et al., 2001) or serpentinites (Blanco–Quintero et al., 2011) mixed with fluid along the plate interface in the subduction channel (Cloos and

Shreve, 1988; Zheng et al., 2011b). The driving forces could be competing drag and buoyancy combined within a convecting fluid (Gerya et al., 2002; Blanco–Quintero et al., 2011; Zheng et al., 2012). For instance, eclogite from the Chinese western Tianshan records a polycyclic burial–partial exhumation evolution that was interpreted to be due to convective flow in the subduction channel (Li et al., 2016).

In this study, we interpret the multiple burial and partial exhumation cycles of eclogite at Sidaohe to be formed in a continental subduction channel. A crustal slice containing the eclogite may have been detached from the surface of the descending lower plate due to fracturing. After the crust had been subducted to a depth of ~100 km, a slice was detached and partially exhumed to ~82 km depth, before being subducted again to a depth of ~107 km. This polycyclic movement may have proceeded due to convective flow in the channel. Metasedimentary rocks, well-exposed in western Dabie, may have acted as a weak, low-viscosity material along the plate interface (Cloos, 1982; Lister et al., 2001; Gerya et al., 2002). In addition, dehydroxylation of NAMs and fluid ingress into eclogite, as discussed above, may facilitate convective movement of rock fragments in the continental subduction channel (Zheng et al., 2011b).

Our study indicates that information for polycyclic *P*–*T* evolution could be potentially preserved in garnet from low *T* eclogite. Especially Ca may preserve prograde chemical variation considering its larger ionic size and lower diffusivity than the other divalent cations. By combining garnet zoning profile and phase equilibrium modeling, we regard more rocks showing polycyclic *P*–*T* evolution could be revealed in further studies.

Thermal relaxation during exhumation

The exhumation P–T path shows an increase in T from the $P_{\max}$ to $T_{\max}$ stages, followed by a decrease of both P and T (Fig. 11). The exhumation path depends on the balance between the rates of exhumation and temperature increase (Carswell and Zhang, 1999). In the early stages of exhumation, unless the exhumation rate is exceedingly fast, deeply subducted rocks may continue to experience heating, resulting in the $T_{\max}$ after the $P_{\max}$ along the exhumation path (Carswell and Zhang, 1999). Such a process has been anticipated by thermal modeling of subducted crustal slabs (England and Thompson, 1984). The increase in T after the $P_{\max}$ is generally interpreted to be due to thermal relaxation by conductive heat transfer (Carswell and Zhang, 1999; Winter, 2013). For deeply subducted continental crust, conductive heating driven by relaxation of isotherms may operate on timescales of tens of Ma (England and Thompson, 1984). Large UHP terranes with ancient crustal protoliths may experience UHP metamorphism over long timescales with slow exhumation rates, while small UHP terranes commonly with juvenile crustal protoliths may experience UHP metamorphism over short timescales with rapid exhumation rates (Kylander–Clark et al., 2012; Zheng et al., 2019). As one of the largest UHP terranes on Earth, the Dabie–Sulu orogen has a metamorphic duration of 15 ± 2 Ma at subarc depths (Wu and Zheng, 2013; Zheng et al., 2019). Therefore, in western Dabie, the relatively long duration of HP/UHP rocks at mantle depths may be sufficient for thermal relaxation during initial exhumation.

ACKNOWLEDGEMENT

We thank associate editor David Dolejs and two anonymous reviewers for their helpful and constructive review comments that have substantially improved the manuscript and Michael Brown for his review on the original manuscript. This study was financially supported by the National Natural Science Foundation of China (41930215) and the Fundamental Research Funds for the Central Universities, China University of Geosciences (Wuhan).

REFERENCES

Anderson, E.D., and Moecher, D.P. (2007) Omphacite breakdown reactions and relation to eclogite exhumation rates. Contributions to Mineralogy and Petrology, 154(3), 253–277.

Beltrando, M., Hermann, J., Lister, G., and Compagnoni, R. (2007) On the evolution of orogens: Pressure cycles and deformation mode switches. Earth and Planetary Science Letters, 256(3–4), 372–388.

Blanco–Quintero, I.F., Garcia–Casco, A., and Gerya, T.V. (2011) Tectonic blocks in serpentinite mélange (eastern Cuba) reveal large-scale convective flow of the subduction channel. Geology, 39(1), 79–82.

Bovay, T., Lanari, P., Rubatto, D., Smit, M., Piccoli, F., and Baldwin, J. (2021) Pressure–temperature–time evolution of subducted crust revealed by complex garnet zoning (Theodul Glacier Unit, Switzerland). Journal of Metamorphic Geology, 10.1111/jmg.12623.

Böhnke, M., Bröcker, M., Maulana, A., Klemd, R., Berndt, J., and Baier, H. (2019) Geochronology and Zr-in-rutile thermometry of high-pressure/low temperature metamorphic rocks from the Bantimala complex, SW Sulawesi, Indonesia. Lithos, 324–325, 340–355.

Brueckner, H. K. (2006) Dunk, dunkless and re-dunk tectonics: A model for metamorphism, lack of metamorphism, and repeated metamorphism of HP/UHP terranes. International Geological Review, 48, 978–995.

Butler, J.P., Beaumont, C., and Jamieson, R.A. (2013) The Alps 1: A working geodynamic model for burial and exhumation of (ultra)high-pressure rocks in Alpine-type orogens. Earth and Planetary Science Letters, 377-378, 114-131.

Caddick, M.J., Konopásek, J., and Thompson, A.B. (2010) Preservation of garnet growth zoning and the duration of prograde metamorphism. Journal of Petrology, 51(11), 2327 –2347.

Carswell, D.A., and Zhang, R.Y. (1999) Petrographic characteristics and metamorphic evolution of ultrahigh-pressure eclogites in plate-collision Belts. International Geology Review, 41(9), 781–798.

Chakraborty, S., and Ganguly, J., 1991. Compositional zoning and cation diffusion in garnets. In: Ganguly, J. (ed.) Diffusion, Atomic Ordering, and Mass Transport. New York: Springer, pp. 120–175.

Chen, R.X., Zheng, Y.F., Gong, B., Zhao, Z.F., Gao, T.S., Chen, B., and Wu, Y.B. (2007) Origin of retrograde fluid in ultrahigh-pressure metamorphic rocks: Constraints from mineral hydrogen isotope and water content changes in eclogite–gneiss transitions in the Sulu orogen. Geochimica et Cosmochimica Acta, 71(9), 2299–2325.

Cheng, H., and Cao, D. (2015) Protracted garnet growth in high-P eclogite: constraints from multiple geochronology and P–T pseudosection. Journal of Metamorphic Geology, 33(6), 613–632.

Cloos, M., and Shreve, R.L. (1988) Subduction-channel model of prism accretion, melange formation, sediment subduction, and subduction erosion at convergent plate margins: 2. Implications and discussion. Pure and applied geophysics, 128(3–4), 501–545.

England, P.C., and Thompson, A.B. (1984) Pressure–temperature–time paths of regional metamorphism I. Heat transfer during the evolution of regions of thickened continental crust. Journal of Petrology, 25, 894–928.

Gerya, T., and Ckhert, B.S. (2006) Two-dimensional numerical modeling of tectonic and metamorphic histories at active continental margins. International Journal of Earth Sciences, 95, 250–274.

Gerya, T.V., Stöckhert, B., and Perchuk, A.L. (2002) Exhumation of high-pressure metamorphic rocks in a subduction channel: A numerical simulation. Tectonics, 21(6), 6–1–6–19.

Godard, G. (2009) Two orogenic cycles recorded in eclogite-facies gneiss from the southern Armorican Massif (France). European Journal of Mineralogy, 21(6), 1173–1190.

Green, E.C.R., White, R.W., Diener, J.F.A., Powell, R., and Holland, T.J.B. (2016) Activity–composition relations for the calculation of partial melting equilibria in metabasic rocks. Journal of Metamorphic Geology, 34, 845–869.

Groppo, C., Rolfo, F., Liu, Y., Deng, L., and Wang, A. (2015) P-T evolution of elusive UHP eclogites from the Luotian dome (North Dabie Zone, China): How far can the thermodynamic modeling lead us? Lithos, 226, 183-200.

Hacker, B.R., Ratschbacher, L., Webb, L.E., McWilliams, M.O., Ireland, T., Calvert, A., Dong, S., Wenk, H.R., and Chateigner, D. (2000) Exhumation of ultrahigh-pressure continental crust in east central China: Late Triassic–Early Jurassic tectonic unroofing. Journal of Geophysical Research, 105(B6), 13339–13364.

Harris, C.R., Hoisch, T.D., and Wells, M.L. (2007) Construction of a composite pressure–temperature path: revealing the synorogenic burial and exhumation history of the Sevier hinterland, USA. Journal of Metamorphic Geology, 25(8), 915–934.

Hawthorne, F. C., Oberti, R., Harlow, G. E., Maresch, W. V., Martin, R. F., Schumacher, J. C. and Welch, M. D. (2012) Nomenclature of the amphibole supergroup. American Mineralogist, 97(11–12), 2031–2048.

Holland, T., and Blundy, J. (1994) Non-ideal interactions in calcic amphiboles and their bearing on amphibole-plagioclase thermometry. contrib Mineral Petr, 116(4), 433-447.

Holland, T., and Powell, R. (2003) Activity–composition relations for phases in petrological calculations: an asymmetric multicomponent formulation. Contributions to Mineralogy and Petrology, 145(4), 492–501.

Holland, T.J.B., and Powell, R. (2011) An improved and extended internally consistent thermodynamic dataset for phases of petrological interest, involving a new equation of state for solids. Journal of Metamorphic Geology, 29(3), 333–383.

Jiao, S., Evans, N. J., Guo, J., Fitzsimons, I. C. W., Zi, J., and McDonald, B. J., 2021. Establishing the P–T path of UHT granulites by geochemically distinguishing peritectic from retrograde garnet. American Mineralogist, 106(10), 1640–1653.

Joanny, V., Van Roermund, H., and Lardeaux, J.M. (1991) The clinopyroxene/plagioclase symplectite in retrograde eclogites: a potential geothermobarometer. Geologische Rundschau, 2, 303–320.

Katayama, I., and Nakashima, S. (2003). Hydroxyl in clinopyroxene from the deep subducted crust: evidence for H_2O transport into the mantle. American Mineralogist, 88, 229–234

Kessel, R., Ulmer, P., Pettke, T., Schmidt, M.W., and Thompson, A.B. (2005) The water–basalt system at 4 to 6 GPa: Phase relations and second critical endpoint in a K-free eclogite at 700 to 1400 °C. Earth and Planetary Science Letters, 237(3–4), 873–892.

Kylander-Clark, A.R.C., Hacker, B.R. and Mattinson, J.M. (2008) Slow exhumation of UHP terranes: titanite and rutile ages of the Western Gneiss Region, Norway. Earth and Planetary Science Letters, 272, 531–540.

Lanari, P., Riel, N., Guillot, S., Vidal, O., Schwartz, S., Pecher, A., and Hattori, K. H.,

2013. Deciphering high-pressure metamorphism in collisional context using microprobe mapping methods: Application to the Stak eclogitic massif (northwest Himalaya). Geology, 41(2), 111–114.

Li, J.L., Klemd, R., Gao, J., and John, T. (2016) Poly-cyclic metamorphic evolution of eclogite: evidence for multistage burial–exhumation cycling in a subduction channel. Journal of Petrology, 57(1), 119–146.

Li, Z., Li, Y., Wijbrans, J.R., Yang, Q., Qiu, H., Brouwer, F.M. (2018) Metamorphic P-T path differences between the two UHP terranes of Sulu orogen, eastern China: petrologic comparison between eclogites from Donghai and Rongcheng. Journal of Earth Science, 29(5): 1151–1166.

Lister, G. S., Forster, M. A., and Rawling, T. J. (2001) Continental Reactivation and Reworking. Geological Society of London, 184, 89–113.

Liu, J., Ye, K., and Sun, M. (2006) Exhumation P–T path of UHP eclogites in the Hong'an area, western Dabie Mountains, China. Lithos, 89(1–2), 154–173.

Liu, Y.S., Hu, Z.C., Gao, S., Günther, D., Xu, J., Gao, C.G. and Chen, H.H. (2008). In situ analysis of major and trace elements of anhydrous minerals by LA-ICP-MS without applying an internalstandard. Chemical Geology 257, (1–2), 34–43.

Liu, X., Jahn, B., Liu, D., Dong, S., and Li, S. (2004) SHRIMP U–Pb zircon dating of a metagabbro and eclogites from western Dabieshan (Hong'an Block), China, and its tectonic implications. Tectonophysics, 394(3–4), 171–192.

Liu, X.C., Wu, Y.B., Gao, S., Wang, J., Peng, M., Gong, H.J., Liu, Y.S., and Yuan, H.L.

(2011) Zircon U–Pb and Hf evidence for coupled subduction of oceanic and continental crust during the Carboniferous in the Huwan shear zone, western Dabie orogen, central China. Journal of Metamorphic Geology, 29(2), 233–249.

Locock, A. J. (2014) An Excel spreadsheet to classify chemical analyses of amphiboles following the IMA 2012 recommendations. Computers & Geosciences, 62, 1–11.

Lou, Y., Wei, C., Liu, X., Zhang, C., Tian, Z., and Wang, W. (2013) Metamorphic evolution of garnet amphibolite in the western Dabieshan eclogite belt, Central China: Evidence from petrography and phase equilibria modeling. Journal of Asian Earth Sciences, 63(0), 130–138.

Martin, C. (2019) P–T conditions of symplectite formation in the eclogites from the Western Gneiss Region (Norway). Geological Society, London, Special Publications, 478(1), 197-216.

O'Brien, P. J., 1997. Garnet zoning and reaction textures in overprinted eclogites, Bohemian Massif, European variscides: a record of their thermal history during exhumation. Lithos, 41(1), 119–133.

Ratschbacher, L., Franz, L., Jonckheere, R., Porschke, A., Hacker, B., Dong, S., and Zhang, Y. (2006) The Sino Korean–Yangtze suture, the Huwan detachment, and the Paleozoic–Tertiary exhumation of (ultra)high-pressure rocks along the Tongbai–Xinxian–Dabie Mountains. Geological Society of America Bulletin, 403, 45–75.

Rubatto, D., Regis, D., Hermann, J., Boston, K., Engi, M., Beltrando, M., and McAlpine, S.R.B. (2011) Yo–yo subduction recorded by accessory minerals in the Italian

Western Alps. Nature Geoscience, 4(5), 338–342.

Schmid, R., Franz, L., Oberhänsli, R., and Dong, S., 2000. High-Si phengite, mineral chemistry and P–T evolution of ultra-high-pressure eclogites and calc-silicates from the Dabie Shan, eastern China. Geological Journal, 35(3–4), 185–207.

Schmidt, M. (1992) Amphibole composition in tonalite as a function of pressure: an experimental calibration of the Al-in-hornblende barometer. Contributions to Mineralogy and Petrology, 110(2–3), 304–310.

Schmidt, M.W., and Poli, S. (2014) Devolatilization during subduction. In: Rudnick, R.L. (ed.) Treatise on Geochemistry, Volume 4: The Crust. Elsevier, Amsterdam, 669–701.

Schwandt, C. S., Cygan, R. T. & Westrich, H. R. (1996). Ca self-diffusion in grossular garnet. American Mineralogist 81, 448–451.

Shreve, R.L., and Cloos, M. (1986) Dynamics of sediment subduction, mélange formation, and prism accretion. Journal of Geophysical Research: Solid Earth, 91(B10), 10229–10245.

Suo, S., Zhong, Z., Zhou, H., You, Z., Zhang, L. (2012) Two fresh types of eclogites in the Dabie–Sulu UHP metamorphic belt, China: implications for the deep subduction and earliest stages of exhumation of the continental crust. Journal of Earth Science, 23(6): 775–785.

Syracuse, E.M., van Keken, P.E., and Abers, G.A. (2010) The global range of subduction zone thermal models. Physics of the Earth and Planetary Interiors, 183(1–2), 73–90.

Taylor–Jones, K., and Powell, R. (2015) Interpreting zirconium-in-rutile thermometric results. Journal of Metamorphic Geology, 33(2), 115–122.

Tomkins, H.S., Powell, R., and Ellis, D.J. (2007) The pressure dependence of the zirconium-in-rutile thermometer. Journal of Metamorphic Geology, 25(6), 703–713.

Vielzeuf, D., Baronnet, A., Perchuk, A.L., Laporte, D., and Baker, M.B. (2007) Calcium diffusivity in alumino-silicate garnets: an experimental and ATEM study. Contributions to Mineralogy and Petrology, 154(2), 153–170.

Wang, J.M., Lanari, P., Wu, F.Y., Zhang, J.J., Khanal, G. P., and Yang, L., 2021. First evidence of eclogites overprinted by ultrahigh temperature metamorphism in Everest East, Himalaya: Implications for collisional tectonics on early Earth. Earth and Planetary Science Letters, 558, 116760.

Waters, D., 2003, P-T path from Cpx-Hbl-Pl symplectites, updated 22 February 2003: http://www.earth.ox.ac.uk/~davewa/research/eclogites/symplectites.html (July 2012).

Wei, C.J., Li, Y.J., Yu, Y., and Zhang, J.S. (2010) Phase equilibria and metamorphic evolution of glaucophane-bearing UHP eclogites from the Western Dabieshan Terrane, Central China. Journal of Metamorphic Geology, 28(6), 647–666.

Wei, C., and Zheng, Y. 2020. Metamorphism, fluid behavior and magmatism in oceanic subduction zones. Science China Earth Sciences, 63: 52–77.

White, R.W., Powell, R., Holland, T.J.B., Johnson, T.E., and Green, E.C.R. (2014) New mineral activity–composition relations for thermodynamic calculations in metapelitic systems. Journal of Metamorphic Geology, 32(3), 261–286.

Whitney, D.L., and Evans, B.W. (2010) Abbreviations for names of rock-forming minerals. American Mineralogist, 95(1), 185–187.

Winter, J.D. (2013) Principles of Igneous and Metamorphic Petrology. Pearson Prentice Hall, Upper Saddle River.

Wu, Y., and Zheng, Y. (2013) Tectonic evolution of a composite collision orogen: An overview on the Qinling–Tongbai–Hong'an–Dabie–Sulu orogenic belt in central China. Gondwana Research, 23(4), 1402–1428.

Wu, Y., Hanchar, J.M., Gao, S., Sylvester, P.J., Tubrett, M., Qiu, H., Wijbrans, J.R., Brouwer, F.M., Yang, S., Yang, Q., Liu, Y., and Yuan, H. (2009) Age and nature of eclogites in the Huwan shear zone, and the multi-stage evolution of the Qinling–Dabie–Sulu orogen, central China. Earth and Planetary Science Letters, 277(3–4), 345–354.

Xia, B., Brown, M., and Zhang, L. (2020) P–T evolution and tectonic significance of lawsonite-bearing schists from the eastern segment of the southwestern Tianshan, China. Journal of Metamorphic Geology, 38(9), 935–962.

Xia, B., Brown, M., Wang, L., Wang, S., and Piccoli, P. (2018a) Phase equilibrium modeling of MT–UHP eclogite: a case study of coesite eclogite at Yangkou Bay, Sulu Belt, Eastern China. Journal of Petrology, 59(7), 1253–1280.

Xia, B., Yang, Q., Chen, N., and Zhou, Z., 2018b. Phase Equilibrium Modeling of Retrograded Eclogite at the Kekesu Valley, Eastern Segment of SW Tianshan

Orogen and Tectonic Implications. Journal of Earth Science, 29, 1060–1073.

Xia, Q.K., Sheng, Y.M., Yang, X.Z., and Yu, H.M. (2005) Heterogeneity of water in garnets from UHP eclogites, eastern Dabieshan, China. Chemical Geology, 224(4), 237–246.

Yan, Q., Zhong, Z., and Zhou, H. (2005) Petrology of Sidaohe area in the UHP metamorphic terrane, the Dabie Mountains. Acta Petrologica et Mineralogica, 24(3), 186-196. (in Chinese with English abstract)

Zhang, G., Ellis, D.J., Christy, A.G., Zhang, L., and Song, S. (2010) Zr-in-rutile thermometry in HP/UHP eclogites from Western China. Contributions to Mineralogy and Petrology, 160(3), 427–439.

Zhang, R., and Liou, J.G. (1994) Coesite-bearing eclogite in Henan Province, central China: detailed petrography, glaucophane stability and PT–path. European Journal of Mineralogy, 6(2), 217–234.

Zhang, R.Y., Liou, J.G., and Ernst, W.G. (2009) The Dabie–Sulu continental collision zone: a

Zheng, Y., and Chen, Y. (2016) Continental versus oceanic subduction zones. National Science Review, 3(4), 495–519.

Zheng, Y., Zhao, Z., and Chen, R. (2019) Ultrahigh–pressure metamorphic rocks in the Dabie–Sulu orogenic belt: compositional inheritance and metamorphic modification. Geological Society, London, Special Publications, 474(1), 89–132.

Zheng, Y.F. (2009) Fluid regime in continental subduction zones: petrological insights from ultrahigh-pressure metamorphic rocks. Journal of the Geological Society, 166(4), 763–782.

Zheng, Y.F., Gao, X.Y., Chen, R.X., and Gao, T.S. (2011a) Zr-in-rutile thermometry of eclogite in the Dabie orogen: Constraints on rutile growth during continental subduction-zone metamorphism. Journal of Asian Earth Sciences, 40(2), 427–451.

Zheng, Y.F., Xia, Q.X., Chen, R.X., and Gao, X.Y. (2011b) Partial melting, fluid supercriticality and element mobility in ultrahigh-pressure metamorphic rocks during continental collision. Earth–Science Reviews, 107(3–4), 342–374.

Zheng, Y.F., Zhang, L.F., McClelland, W.C., and Cuthbert, S. (2012) Processes in continental collision zones: preface. Lithos, 136–139(0), 1–9.

FIGURE CAPTIONS

Figure 1. **(a)** Tectonic framework of the Sulu–Dabie orogen in central China. It is located between the Yangtze craton to the south and the Sino–Korean craton to the north; **(b)** Geological map of the western Dabie (modified from Wei et al., 2010). Based on lithologies and metamorphic grade, western Dabie is subdivided into 6 units. From south to north, they are: the Mulanshan greenschist–blueschist unit, the Hong'an HP eclogite unit, the Xinxian UHP eclogite unit, the Huwan HP eclogite unit, the Balifan mélange unit and the Nanwan flysch unit.

Figure 2. **(a)** Eclogitic block enclosed in the host garnet-bearing felsic gneiss. Eclogite is strongly retrogressed from the center towards the rim. Abundant quartz veins are at the edge of the block, with less in its interior; **(b)** Small veinlets in the center of the block

where eclogite Sdh–1 was sampled. Close to veinlet, eclogite was more strongly retrogressed; **(c)** Thin section for Sdh–1 showing bimineralic texture with omphacite in the matrix completely replaced by Pl ± Amp ± Cpx symplectite; **(d)** Thin section for DB17–06 with veinlet of megacrystal rutile and quartz cross-cutting eclogite.

Figure 3. Photomicrographs showing the mineralogy and microstructures of eclogite in BSE images **(a, b, c, f, l)**, under cross-polarized light **(e)** and plane-polarized light **(d, g, h, i, j, k)**. **(a)** Subhedral garnet porphyroblast from Sdh–1 with inclusions of Ep, Amp, Omp and Qtz; cracks in garnet are mainly filled with Amp + Pl + Rt/Ilm. Traverses of point analyses roughly follow the solid white line; **(b)** Subhedral garnet porphyroblast from Sdh–2. Traverses of point analyses roughly follow the solid white line; **(c)** Omphacite inclusion in garnet of Fig. 3a. Omphacite was partly replaced by Cpx + Pl symplectite (Sym2) which was rimmed by coarse Amp; **(d, e)** Omphacite inclusion in garnet. In the matrix, Pl ± Amp ± Cpx symplectite shows short prismatic or granular shapes interpreted to be pseudomorphs after omphacite; **(f)** Fractures in garnet filled with fibrous Amp + Pl ± Rt/Ilm symplectite; **(g, h)** Cpx + Pl + Amp (Sym1), Cpx + Pl (Sym2) and Amp + Pl (Sym3) symplectites in the matrix showing short prismatic shape; **(i)** Rutile inclusions in garnet (type 1); **(j)** Rutile as single grains in the matrix abutting garnet (type 2); **(k)** Rutile in the matrix surrounded by Qtz + Amp or Pl ± Amp ± Cpx symplectite (type 2); **(l)** Megacrystal rutile in quartz veinlet crosscutting eclogite (type 3). Rutile has been partially replaced by ilmenite along rims or fractures.

Figure 4. Traverses of point analyses for garnet from **(a)** Sdh–1 and **(b)** Sdh–2. Half A

and B represent analyses for one half and the other half of the garnet, respectively; (**c–d**) element mapping of Ca and Mg for a large porphyroblastic garnet from Sdh–1; the dotted lines may represent garnet zoning patterns; (**e–f**) Ca and Mg element mapping for a large porphyroblastic garnet from Sdh–2; the dotted lines represent suggested garnet zoning patterns.

Figure 5. Photomicrographs showing the microstructures of symplectite in Sdh–1 under plane-polarized light **(a)** and in BSE images **(b, c)**. Element maps of Sym1 **(d–f)** and Sym2 **(h–k)** showing intergrowths of Cpx, Pl and/or Amp generally oriented perpendicular to the reaction front. From Sym1 to Sym2, Amp (in volume content) decreases while Cpx increases **(d–k)**.

Figure 6. Compositions of omphacite and amphibole from the eclogite Sdh–1 and Sdh–2. **(a)** Compositions of omphacite. WEF represents endmembers for Wo (wollastonite), En (enstatite) and Fs (ferrosilite) after Morimoto et al., (1988); **(b)** Classification of amphibole with various occurrences (after Hawthorne et al., 2012). Ing, as inclusions in garnet; rimg, rimming garnet.

Figure 7. **(a, c)** *P–T* pseudosection for the eclogite Sdh–1. ① Grt Dio Gln Lws Spn, ②Grt Gln Lws Ep Spn, ③ Grt Gln Lws Dio Omp Ep, ④ Grt Gln Lws Dio Omp Ta, ⑤Grt Lws Omp Ky, ⑥ Grt Gln Omp Ky, ⑦ Grt Gln Omp Ky Ep, ⑧ Grt Gln Omp Ep Spn, ⑨ Grt Gln Lws Dio; **(b, d)** *P–T* pseudosection for the eclogite Sdh–2. ① Grt Dio Gln Lws Spn, ② Grt Gln Lws Ep Spn, ③ Grt Gln Lws Dio Ep, ④ Grt Dio Gln Ep Spn, ⑤ Grt Gln Dio Omp Lws Ep, ⑥ Grt Gln Dio Ep, ⑦ Grt Gln Dio Omp

Lws Ta,⑧Grt Gln Dio Lws, ⑨ Grt Omp Lws; **(e)** Variations of *P* defined by isopleths of Grs in Grt from core to rim; **(f)** Compilation of the inferred *P–T* evolution from the later prograde to the P_{max}, then to the T_{max} stages for both *P–T* pseudosections for Sdh–1 and Sdh–2. The whole rock compositions are given in Table 4. "cg" represents calculated isopleths for Grs in garnet, "mg" represents calculated isopleths for Prp in garnet, xmg represents calculated isopleths for X_{Mg} in garnet and "jo" represents calculated isopleths for j(o) of omphacite. Lws-Ec represents lawsonite eclogite facies, Ep-Ec represents epidote eclogite facies, Amph-Ec represents amphibolite facies, Ep-Bs represents epidote blueschist facies, EA represents epidote amphibolite facies, AM represents amphibolite facies, HGR represents high pressure granulite facies (after Liou et al., 2004). In this study, according to *a–x* models of amphibole for modeling phase diagram using Thermocalc, glaucophane is defined to have high z (0.8–1, Na on the M4 site) and y (0.9–1, octahedral Al) combined with low a (0–0.2, A-site Na) and c (0–0.2, Ca), whereas hornblende is defined to have high a (0.2–0.6), y (0.2–0.6) and c (0.6–0.9).

Figure 8. **(a)** *P–T* and **(b)** $P–M_{H2O}$ pseudosections for the eclogite Sdh–1. The whole rock compositions are given in Table 4. "jo" represents calculated isopleths for j(o) of omphacite.

Figure 9. **(a–c)** Nb/Ta vs Nb, Ta and Zr, and **(d–f)** Zr vs Sc, U and Hf characteristics for rutile with various occurrences.

Figure 10. The calculated *T* using the Zr-in-rutile thermometer by Tomkins et al. (2007)

for rutile with various occurrences. **(a)** Calculated at 25.0–30.0 kbar for type 1 rutile; **(b)** Calculated at 25.0–20.0 kbar for type 2 rutile; (c) Calculated at 15.0–10.0 kbar for type 3 rutile and summary of the T calculated for rutile with various occurrences; **(d)** The interquartile T range for rutile with various occurrences. Box represents the interquartile *T* range. The thick black line in the rhombic field from a–c represents the upper limit of the interquartile *T* range.

Figure 11. Summary of *P–T* paths from this and previous studies of eclogite from western Dabie. The purple arrows represent the *P–T* path from our study. The solid arrow was inferred from garnet compositional isopleth thermobarometry; the dashed arrow was inferred from a combination of phase equilibrium modeling, Zr-in-rutile thermometer (blue rhombus) and Hb–Pl thermobarometry (green diamond).

Table 1. Representative compositions of garnet from eclogite at Sidaohe, western Dabie.

sample	Sdh-1						Sdh-2					
mineral	Grt	Grt	Grt	Grt	Grt	Grt	Grt	Grt	Grt	Grt	Grt	Grt
position	r	r	r	c	c	c	r	r	r	c	c	c
SiO_2	39.00	39.25	39.44	39.57	39.33	39.33	39.18	38.13	39.35	39.13	39.30	39.40
TiO_2	bd	0.03	0.04	0.13	0.10	0.05	0.06	0.04	0.06	0.12	0.22	0.06
Al_2O_3	21.57	21.50	21.43	21.11	21.51	20.96	21.38	20.72	21.35	21.08	21.16	21.24
Cr_2O_3	bd	bd	bd	bd	bd	bd	bd	bd	bd	bd	bd	bd
FeO	25.30	24.56	24.48	23.62	23.50	23.21	24.98	25.00	24.04	24.19	23.69	23.64
MnO	0.65	0.53	0.51	0.74	0.68	0.58	0.55	0.53	0.55	0.65	0.58	0.58
MgO	6.04	5.65	5.66	5.02	5.17	4.81	5.74	5.67	5.13	5.21	5.09	5.07
CaO	7.38	8.95	9.26	10.16	10.36	11.13	8.22	8.49	9.60	9.74	10.04	10.72
Na_2O	0.01	0.01	0.04	0.04	0.05	0.03	0.04	0.04	0.05	0.04	0.03	0.01
K_2O	bd	bd	bd	bd	bd	0.01	bd	bd	0.01	0.01	bd	bd
Totals	99.94	100.48	100.85	100.39	100.69	100.10	100.16	98.61	100.13	100.17	100.12	100.72
Oxygens	12.00	12.00	12.00	12.00	12.00	12.00	12.00	12.00	12.00	12.00	12.00	12.00

Si	3.02	3.03	3.03	3.06	3.03	3.05	3.03	3.00	3.04	3.04	3.04	3.04
Ti	bd	0.00	0.00	0.01	0.01	0.00	0.00	0.00	0.00	0.01	0.01	0.00
Al	1.97	1.96	1.94	1.92	1.95	1.92	1.95	1.92	1.95	1.93	1.93	1.93
Cr	bd	bd	bd	bd	bd	bd	bd	bd	bd	bd	bd	bd
Fe^{3+}	0.00	0.00	0.00	0.00	0.00	0.00	0.00	0.07	0.00	0.00	0.00	0.00
Fe^{2+}	1.64	1.58	1.57	1.53	1.51	1.50	1.62	1.58	1.56	1.57	1.53	1.52
Mn	0.04	0.04	0.03	0.05	0.04	0.04	0.04	0.04	0.04	0.04	0.04	0.04
Mg	0.70	0.65	0.65	0.58	0.59	0.56	0.66	0.67	0.59	0.60	0.59	0.58
Ca	0.61	0.74	0.76	0.84	0.85	0.92	0.68	0.72	0.80	0.81	0.83	0.89
Na	0.00	0.00	0.01	0.01	0.01	0.00	0.01	0.01	0.01	0.01	0.01	0.00
K	bd	bd	bd	bd	bd	0.00	bd	bd	0.00	0.00	bd	bd
Sum	7.99	7.99	8.00	7.98	8.00	7.99	7.99	8.00	7.98	8.00	7.98	8.00
Alm	0.55	0.53	0.52	0.51	0.50	0.50	0.54	0.53	0.52	0.52	0.51	0.50
Prp	0.23	0.22	0.22	0.19	0.20	0.18	0.22	0.22	0.20	0.20	0.20	0.19
Grs	0.21	0.25	0.25	0.28	0.28	0.31	0.23	0.24	0.27	0.27	0.28	0.29
Sps	0.01	0.01	0.01	0.02	0.02	0.01	0.01	0.01	0.01	0.01	0.01	0.01

Note: c, core; r, rim. The mineral formulae were calculated using the program AX (updated in October, 2019; https://filedn.com/lU1GlyFhv3UuXg5E9dbnWFF/TJBHpages/ax.html). bd, below detection.

Table 2. Representative compositions of clinopyroxene, amphibole and plagioclase from eclogite at Sidaohe, western Dabie.

sample					Sdh-1						Sdh-2				
minerals	Omp	Cpx1	Amp	Amp	Amp	Amp	Pl	Pl	Omp	Cpx1	Amp	Amp	Amp	Pl	Pl
position	ing	Sym1	ing	rimg	Sym1	Sym3	Sym1	Sym3	ing	Sym1	ing	Sym1	Sym3	Sym1	Sym3
SiO_2	55.69	53.68	40.67	39.16	43.92	49.19	66.84	68.61	56.44	54.25	42.38	42.20	48.52	67.84	68.57
TiO_2	0.01	0.05	0.21	0.08	0.10	0.32	bd	0.01	0.10	0.19	0.21	0.83	0.46	bd	0.00
Al_2O_3	10.53	4.39	18.85	20.34	11.92	6.72	20.97	19.73	10.35	8.54	14.63	15.12	7.51	20.83	20.16
Cr_2O_3	0.00	0.00	0.01	0.03	bd	bd	bd	bd	0.01	0.03	0.00	0.04	0.14	bd	0.00
FeO	6.19	7.96	14.67	11.84	16.68	13.86	0.24	0.17	6.63	9.25	13.77	14.56	13.10	0.21	0.17
MnO	0.01	0.00	0.11	0.12	0.06	0.07	bd	bd	0.00	0.02	0.28	0.45	0.07	bd	0.02
MgO	8.27	11.78	9.57	11.11	10.56	15.38	bd	0.00	7.62	9.99	12.18	10.98	13.91	bd	0.01
CaO	11.93	18.05	9.15	10.91	11.25	9.90	1.68	0.26	11.81	13.47	9.99	9.68	11.45	1.19	0.35
Na_2O	7.34	2.98	2.59	2.84	2.04	1.17	10.91	11.62	6.80	3.20	2.70	2.50	1.15	11.08	11.74
K_2O	0.00	0.00	bd	0.01	0.04	0.02	0.02	0.02	0.00	0.02	0.02	0.02	0.03	0.01	0.00
Totals	99.95	98.89	95.88	96.44	96.56	96.63	100.68	100.42	99.76	98.97	96.17	96.39	96.33	101.14	101.01
Oxygens	6.00	6.00	23.00	23.00	23.00	23.00	8.00	8.00	6.00	6.00	23.00	23.00	23.00	8.00	8.00
Si	1.98	1.98	6.02	5.73	6.55	7.12	2.91	2.99	2.02	1.98	6.26	6.24	7.09	2.94	2.97
Ti	0.00	0.00	0.02	0.01	0.01	0.04	0.00	0.00	0.00	0.01	0.02	0.09	0.05	bd	0.00
Al	0.44	0.19	3.29	3.51	2.10	1.15	1.08	1.01	0.44	0.37	2.55	2.63	1.29	1.06	1.03
Cr	0.00	0.00	0.00	0.00		bd	bd	bd	0.00	0.00		0.01	0.02	bd	0.00
Fe^{3+}	0.11	0.05	0.46	0.51	0.40	0.54	0.01	0.01	0.00	0.00	0.44	0.42	0.32	0.01	0.01
Fe^{2+}	0.08	0.20	1.36	0.94	1.68	1.14	bd	bd	0.20	0.28	1.27	1.38	1.29	bd	0.00
Mn	0.00	0.00	0.01	0.01	0.01	0.01	bd	0.00	0.00	0.00	0.04	0.06	0.01	bd	0.00

Mg	0.44	0.65	2.11	2.42	2.35	3.32	0.00	0.00	0.41	0.54	2.68	2.42	3.03	0.00	0.00
Ca	0.45	0.72	1.45	1.71	1.80	1.54	0.08	0.01	0.45	0.53	1.58	1.53	1.79	0.06	0.02
Na	0.51	0.21	0.74	0.81	0.59	0.33	0.92	0.98	0.47	0.23	0.77	0.72	0.33	0.93	0.99
K	0.00	0.00	bd	0.00	0.01	0.00	0.00	0.00	0.00	0.00	0.00	0.00	0.01	0.00	0.00
Sum	4.00	4.00	15.46	15.65	15.49	15.17	5.00	5.00	3.99	3.94	15.61	15.50	15.21	4.99	5.01
X_{Mg}	0.45	0.42	0.61	0.72	0.58	0.74			0.38	0.40	0.68	0.64	0.70		
j(o)	0.53	0.23							0.51	0.30					
Ab							0.92	0.99						0.94	0.98

Note: The mineral formulae were calculated using the program AX (Tim Holland's AX software page: http://www.esc.cam.ac.uk/research/research-groups/research-projects/tim-hollands-software-pages/ax) except Amp whose formulae was calculated after Locock (2014) conforming to the IMA guidelines. bd, below detection. ing, inclusions in garnet; rimg, rimming garnet; X_{Mg} = Mg/(Mg+Fe^{2+}); j(o) = Na/(Na+Ca).

Table 3. Representative composition of rutile from eclogite at Sidaohe, western Dabie and calculated *T* using Zr-in-rutile thermometer.

		REE content (ppm)								Zr-in-rutile results (°C)						
sample	position	Nb	Ta	Nb/Ta	Sc	U	Hf	Zr	2σ (Zr)	T10	T20	T25	T30	2σ	Z2004	W2006
Sdh-1	ing	326.9	21.6	15.1	2.2	0.6	3.7	124.3	9.1	583.9	623.8	643.7	659.5	5.5	606.4	577.6
Sdh-1	ing	362.6	22.1	16.4	6.3	1.2	2.8	75.2	6.6	550.3	588.7	607.8	622.5	6.1	542.0	544.1
Sdh-1	ing	350.2	21.3	16.5	3.1	1.1	3.3	100.8	8.1	569.5	608.8	628.4	643.7	5.9	579.6	563.3
Sdh-1	ing	340.8	22.8	14.9	5.9	2.8	3.5	114.2	9.1	578.0	617.6	637.5	653.0	5.9	595.5	571.8
Sdh-1	ing	322.4	18.8	17.2	4.7	0.5	3.7	105.0	7.9	572.3	611.6	631.3	646.7	5.5	584.7	566.0
Sdh-1	ing	330.5	19.3	17.1	4.6	0.4	3.6	89.3	6.4	561.5	600.3	619.8	634.8	5.2	564.0	555.3
Sdh-1	ing	334.7	22.0	15.2	5.0	0.6	3.5	100.7	8.7	569.4	608.7	628.3	643.6	6.3	579.4	563.2
Sdh-1	matrix	466.9	22.2	21.0	5.5	1.5	5.2	152.0	12.6	598.0	638.6	658.9	675.2	6.4	632.1	591.8
Sdh-1	matrix	381.8	22.1	17.3	4.4	1.2	4.5	163.3	10.2	603.2	644.0	664.4	680.9	5.0	641.2	597.0
Sdh-1	matrix	324.3	19.3	16.8	3.9	1.1	3.8	96.3	8.2	566.5	605.6	625.1	640.3	6.2	573.7	560.2
Sdh-1	matrix	383.0	19.0	20.1	3.3	1.7	4.2	160.9	9.1	602.1	642.9	663.3	679.7	4.5	639.3	595.9
Sdh-1	matrix	483.8	29.3	16.5	5.0	2.7	7.1	247.8	16.6	634.5	676.8	697.9	715.6	5.7	694.5	628.3
Sdh-1	matrix	338.6	21.0	16.1	4.2	1.5	5.0	221.3	13.4	625.8	667.7	688.6	705.9	5.1	680.0	619.6
Sdh-1	matrix	356.0	21.3	16.7	4.9	2.5	3.3	135.3	9.2	589.8	630.0	650.1	666.1	5.2	617.2	583.6
Sdh-1	matrix	407.8	19.8	20.6	2.4	2.0	3.1	95.7	7.7	566.1	605.2	624.7	639.9	5.8	572.9	559.8
Sdh-1	matrix	347.7	21.0	16.6	2.5	2.1	3.2	109.2	7.8	575.0	614.5	634.2	649.7	5.3	589.8	568.7
Sdh-1	matrix	364.6	21.9	16.6	3.9	1.0	6.2	189.9	11.2	614.3	655.6	676.3	693.2	4.8	660.5	608.1
Sdh-1	matrix	328.2	19.6	16.7	2.1	0.7	3.6	96.5	7.5	566.6	605.7	625.3	640.5	5.7	574.0	560.4
Sdh-1	matrix	342.1	20.5	16.7	1.8	0.9	4.1	102.4	7.2	570.6	609.9	629.6	644.9	5.2	581.6	564.4
Sdh-1	matrix	393.0	21.2	18.5	2.4	0.6	5.6	150.8	10.2	597.4	638.0	658.3	674.6	5.3	631.0	591.2
DB17-06	mega	336.7	19.4	17.3	1.2	0.7	4.0	83.7	6.2	557.2	595.9	615.2	630.1	5.2	555.7	551.0
DB17-06	mega	376.8	21.8	17.3	1.2	0.9	3.9	96.6	6.0	566.7	605.8	625.4	640.6	4.5	574.1	560.5
DB17-06	mega	339.7	20.0	17.0	1.3	0.5	3.7	86.9	6.4	559.7	598.5	617.9	632.8	5.3	560.6	553.5

DB17-06	mega	354.0	22.6	15.6	1.2	0.4	3.9	84.0	5.1	557.5	596.2	615.5	630.4	4.3	556.2	551.3
DB17-06	mega	343.0	20.0	17.2	1.1	0.4	3.4	76.8	4.7	551.7	590.1	609.3	624.0	4.3	544.7	545.4
DB17-06	mega	345.2	18.9	18.3	1.2	0.5	4.4	88.9	5.1	561.2	600.0	619.5	634.5	4.1	563.5	555.0
DB17-06	mega	348.1	15.5	22.5	1.1	0.6	4.5	105.0	7.7	572.3	611.6	631.3	646.7	5.4	584.7	566.1
DB17-06	mega	361.9	26.1	13.9	1.0	0.4	3.9	91.8	6.0	563.3	602.3	621.8	636.9	4.7	567.7	557.1
DB17-06	mega	369.2	20.4	18.1	1.4	0.5	3.5	82.0	4.9	555.9	594.5	613.8	628.6	4.2	553.1	549.7
DB17-06	mega	323.9	19.3	16.8	1.0	6.1	3.6	84.0	5.4	557.5	596.1	615.5	630.4	4.6	556.2	551.2
DB17-06	mega	336.2	19.0	17.7	0.9	0.6	3.9	81.0	5.4	555.1	593.7	613.0	627.8	4.7	551.6	548.9
DB17-06	mega	331.7	17.7	18.7	2.4	0.3	3.3	75.2	5.1	550.4	588.7	607.9	622.5	4.8	542.2	544.2
DB17-06	mega	344.6	18.7	18.4	2.0	0.5	3.4	89.1	7.3	561.3	600.2	619.6	634.6	5.9	563.8	555.1
DB17-06	mega	356.9	19.8	18.0	1.8	0.5	3.6	83.9	4.8	557.4	596.1	615.4	630.3	4.1	556.0	551.2
DB17-06	mega	355.9	22.6	15.8	1.6	0.4	3.5	71.9	4.8	547.5	585.7	604.9	619.4	4.6	536.5	541.3
DB17-06	mega	363.1	21.0	17.3	2.2	0.3	3.6	84.4	6.0	557.8	596.5	615.8	630.7	5.1	556.8	551.6
DB17-06	mega	352.1	17.5	20.1	1.6	0.4	3.6	90.3	6.2	562.2	601.1	620.6	635.6	4.9	565.5	556.0
DB17-06	mega	435.1	26.8	16.2	1.5	0.3	3.6	87.4	7.4	560.1	598.9	618.3	633.3	6.0	561.3	553.9
DB17-06	mega	357.0	20.1	17.8	1.8	4.6	3.6	76.2	5.1	551.2	589.6	608.8	623.4	4.7	543.8	545.0
DB17-06	mega	348.5	18.9	18.4	1.7	0.5	3.4	82.3	6.3	556.2	594.8	614.1	628.9	5.4	553.6	549.9

Note: ing, rutile as inclusions in garnet (type 1); matrix, rutile in the matrix (type 2); meta, megacrystal rutile in quartz veinlet (type 3). T10, *T* calculated at 10.0 kbar using the Zr-in-rutile thermometer calibrated by Tomkins (2007), similar to T20, T25 and T30; Z2004, Zack et al. (2004); W2006, Watson et al. (2006).

Table 4. Whole rock compositions (in wt%) together with modified bulk compositions (in mol%) used for phase diagram calculations for eclogite at Sidaohe, western Dabie. For the modified bulk compositions, FeO^T represents total iron. Oxygen (in mol%) is equal to Fe_2O_3 (in mol%).

Samples	Figures	H_2O	SiO_2	Al_2O_3	CaO	MgO	FeO (FeO^T)	K_2O	Na_2O	TiO_2	MnO	Fe_2O_3 (O)	P_2O_5
Primary bulk rock composition (wt%)													
Sdh-1		*	50.99	13.97	9.54	5.52	14.28	0.03	2.87	2.46	0.22	*	0.39
Sdh-2		*	48.02	13.73	9.99	6.04	14.85	0.04	2.87	2.32	0.21	*	0.43
Corrected bulk rock composition (mol%)													
Sdh-1	Fig. 7a, c	excess	54.53	8.80	10.34	8.80	11.49	0.02	2.97	1.98	0.19	0.86	
	Fig. 8a	excess	57.59	6.18	11.82	10.98	4.80	0.00	5.65	1.99	0.00	0.98	
	Fig. 8b	0.00	57.59	6.18	11.82	10.98	4.80	0.00	5.65	1.99	0.00	0.98	
		2.00	56.43	6.06	11.59	10.76	4.71	0.00	5.54	1.95	0.00	0.96	
Sdh-2	Fig. 7b, d	excess	52.22	8.80	10.98	9.79	12.15	0.03	3.02	1.90	0.19	0.91	

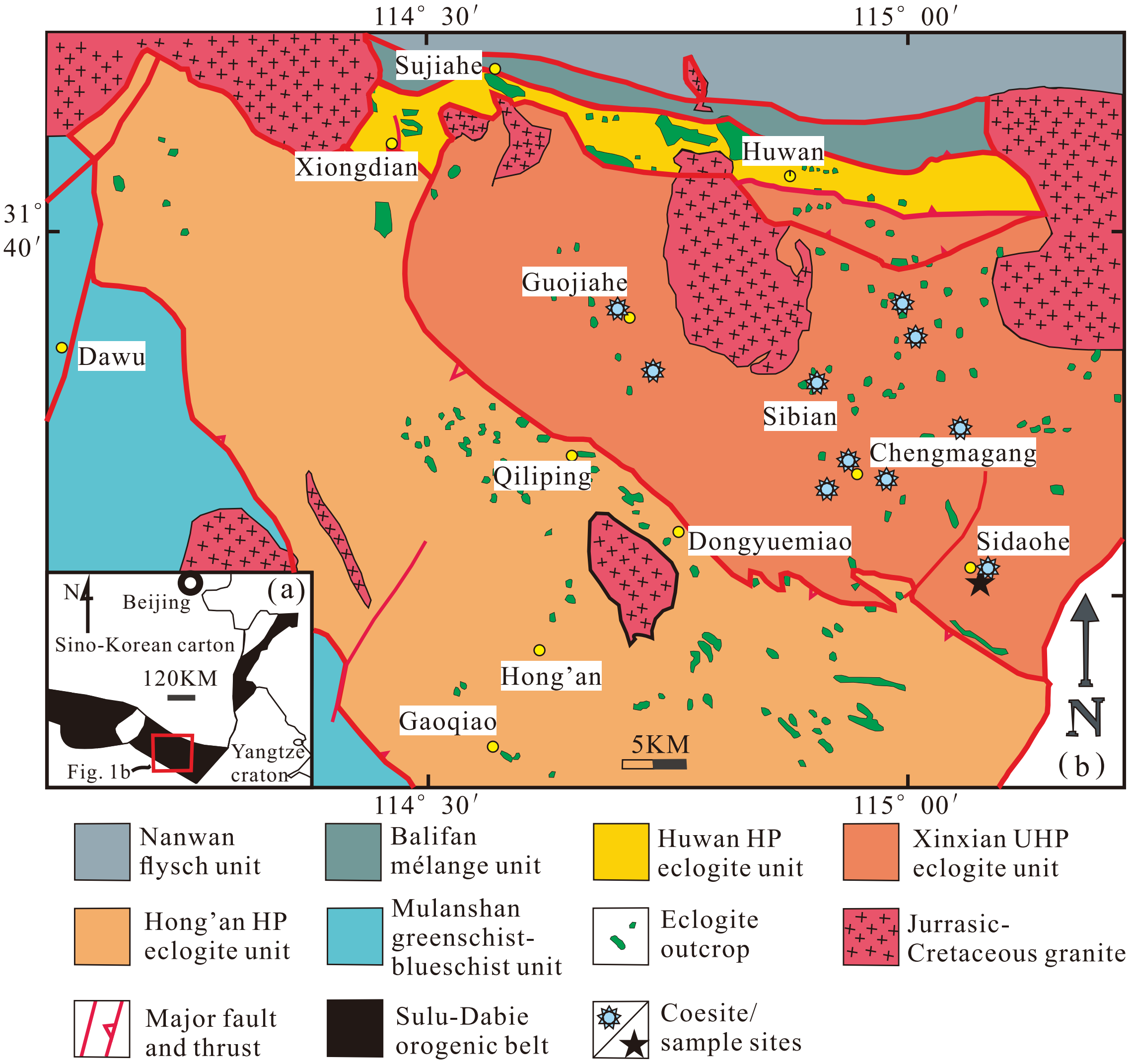
114° 30′
115° 00′
31° 40′
31° 20′
Sujiahe
Xiongdian
Huwan
Guojiahe
Dawu
Sibian
Chengmagang
Qiliping
Dongyuemiao
Sidaohe
Hong'an
Gaoqiao
5KM
N
(b)
N
Beijing
(a)
Sino-Korean carton
120KM
Yangtze craton
Fig. 1b
Nanwan flysch unit
Balifan mélange unit
Huwan HP eclogite unit
Xinxian UHP eclogite unit
Hong'an HP eclogite unit
Mulanshan greenschist-blueschist unit
Eclogite outcrop
Jurrasic-Cretaceous granite
Major fault and thrust
Sulu-Dabie orogenic belt
Coesite/ sample sites

Figure 1

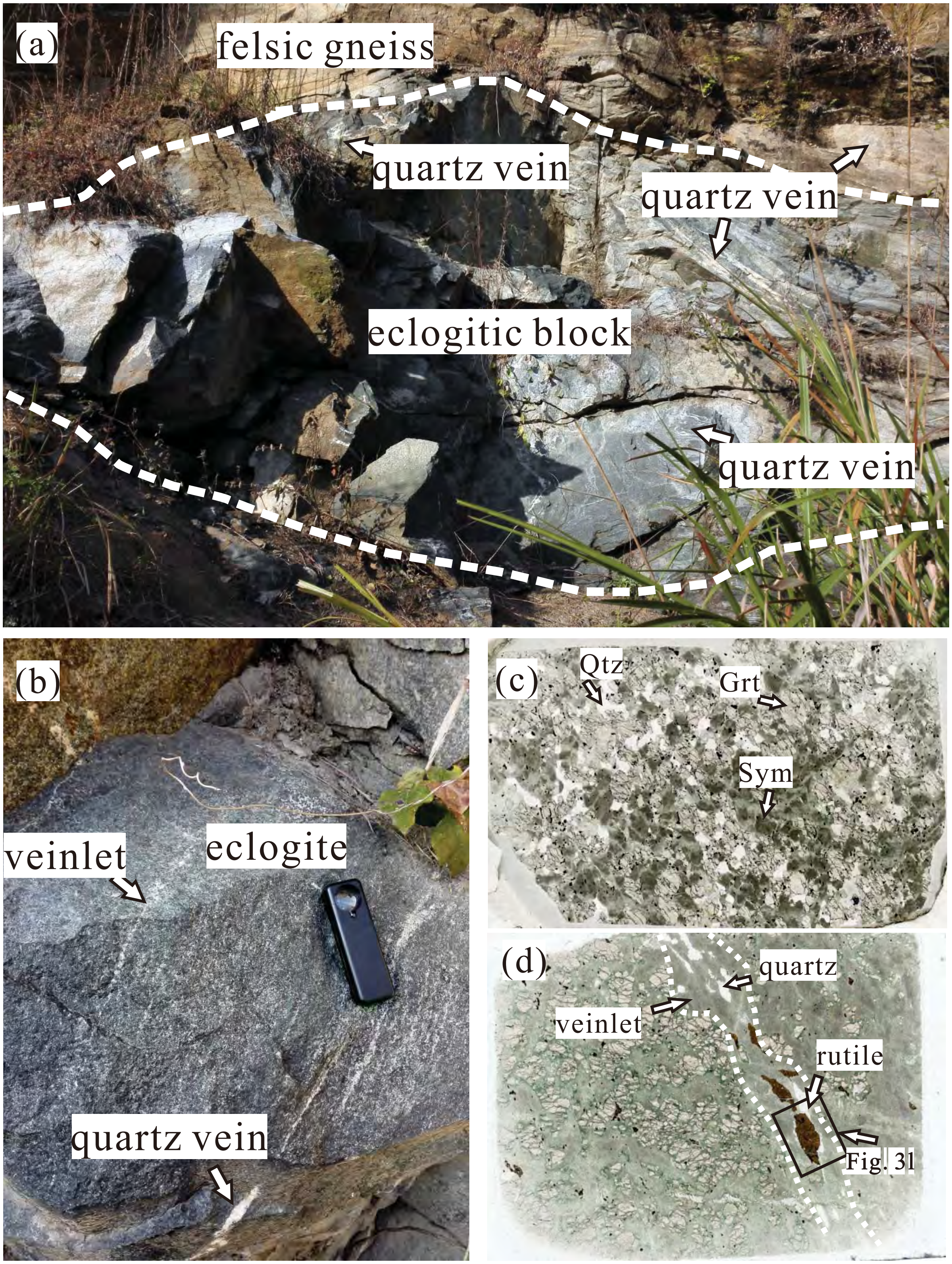
(a)
felsic gneiss
quartz vein
quartz vein
eclogitic block
quartz vein
(b)
veinlet
eclogite
quartz vein
(c)
Qtz
Grt
Sym
(d)
quartz
veinlet
rutile
Fig. 3l

Figure 2

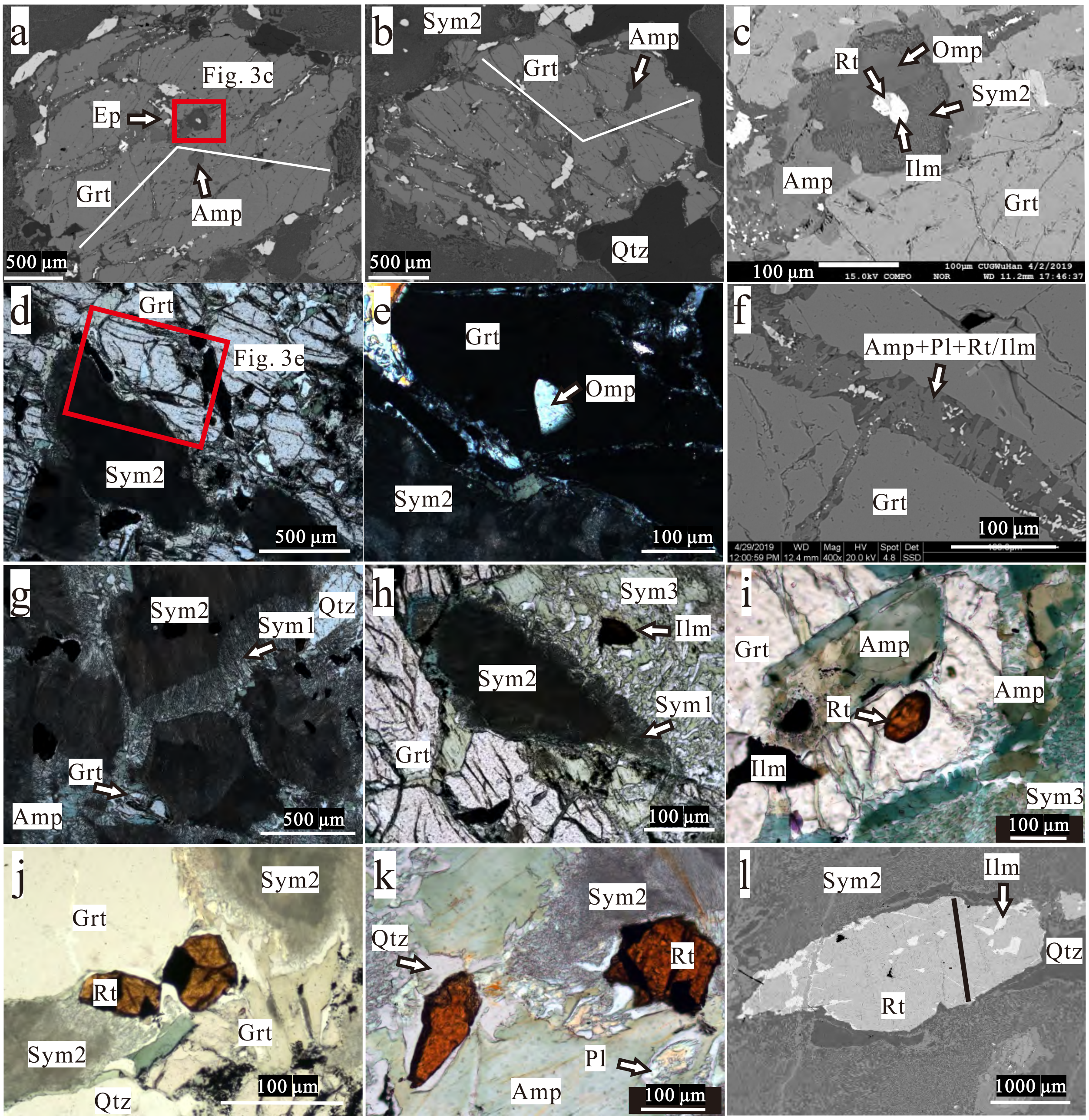
a
Fig. 3c
Ep
Grt
Amp
500 µm
b
Sym2
Amp
Grt
Qtz
500 µm
c
Rt
Omp
Sym2
Ilm
Amp
Grt
100 µm
100µm CUGWuHan 4/2/2019
15.0kV COMPO NOR WD 11.2mm 17:46:37
d
Grt
Fig. 3e
Sym2
500 µm
e
Grt
Omp
Sym2
100 µm
f
Amp+Pl+Rt/Ilm
Grt
100 µm
4/29/2019 12:00:59 PM WD 12.4 mm Mag 400x HV 20.0 kV Spot 4.8 Det SSD
g
Sym2
Sym1
Qtz
Grt
Amp
500 µm
h
Sym3
Ilm
Sym2
Sym1
Grt
100 µm
i
Grt
Amp
Amp
Rt
Ilm
Sym3
100 µm
j
Sym2
Grt
Rt
Grt
Sym2
Qtz
100 µm
k
Sym2
Qtz
Rt
Pl
Amp
100 µm
l
Sym2
Ilm
Qtz
Rt
1000 µm

Figure 3

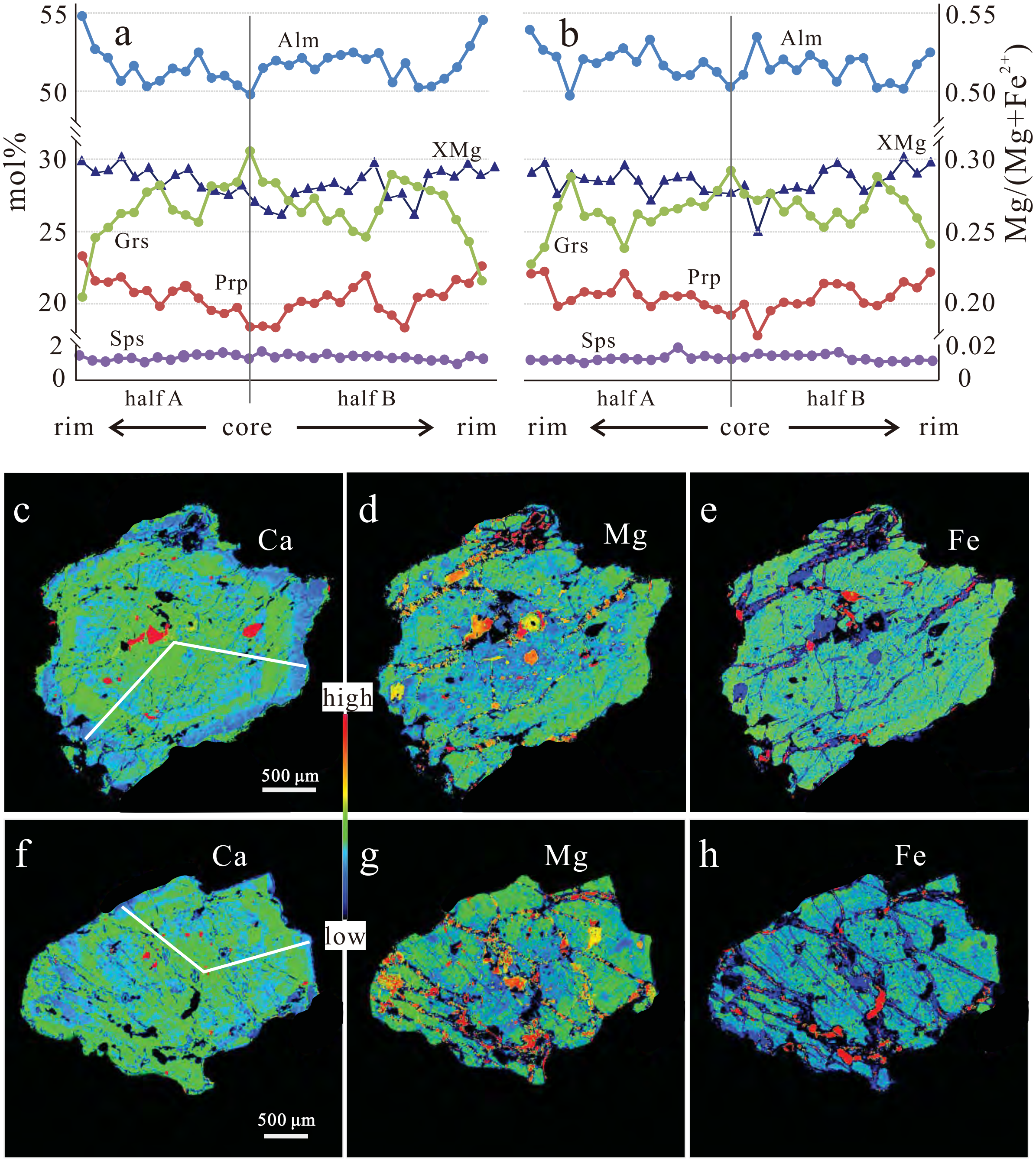
a
b
55
50
30
25
20
2
0
mol%
0.55
0.50
0.30
0.25
0.20
0.02
0
Mg/(Mg+Fe^{2+})
Alm
XMg
Grs
Prp
Sps
half A
half B
rim
core
rim
c
Ca
d
Mg
e
Fe
f
Ca
g
Mg
h
Fe
high
low
500 μm
500 μm

Figure 4

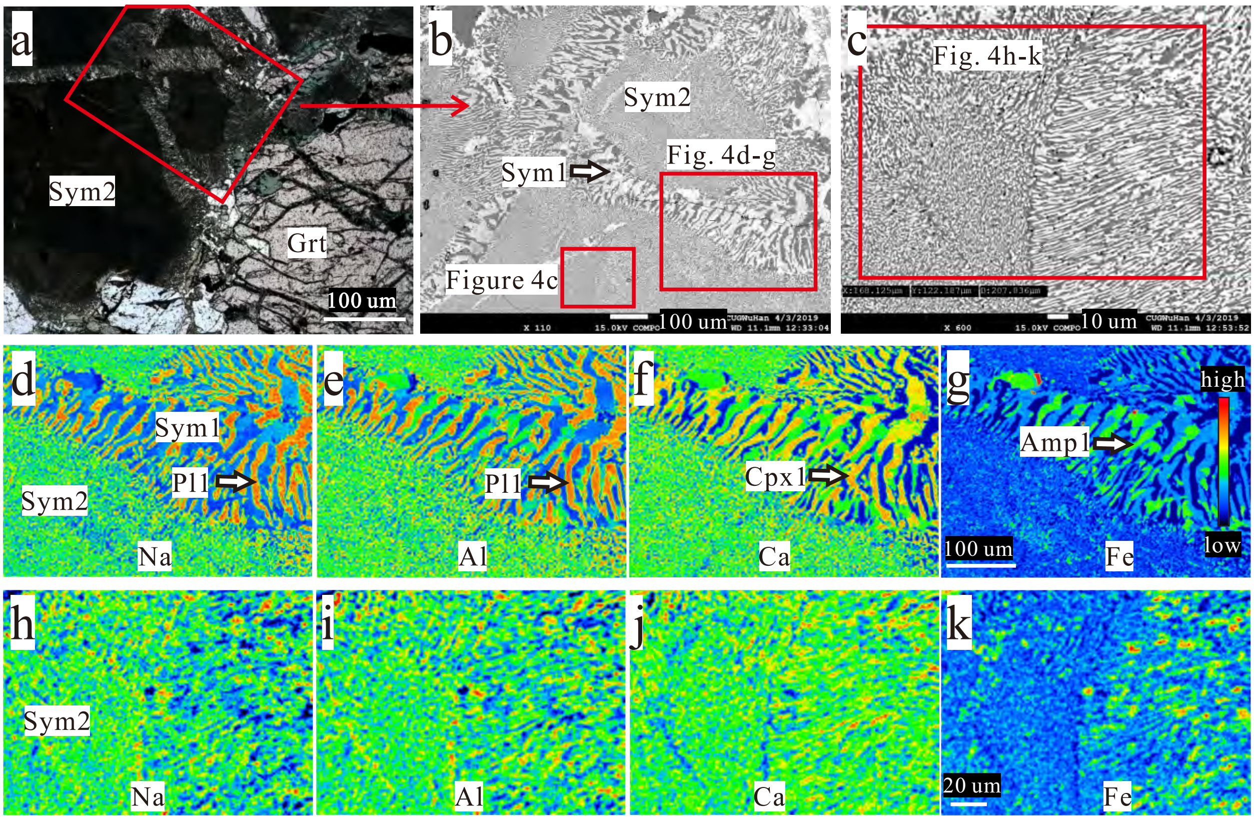
a
Sym2
Grt
100 um
b
Sym2
Sym1
Fig. 4d-g
Figure 4c
100 um
c
Fig. 4h-k
10 um
d
Sym1
Pl1
Sym2
Na
e
Pl1
Al
f
Cpx1
Ca
g
high
Amp1
low
100 um
Fe
h
Sym2
Na
i
Al
j
Ca
k
20 um
Fe

Figure 5

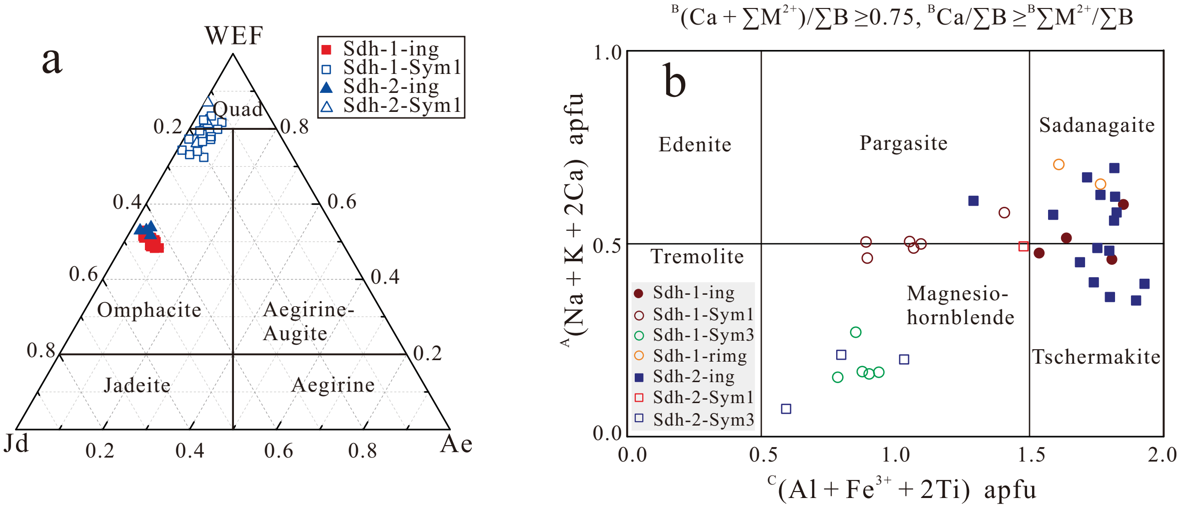
a
WEF
Quad
Omphacite
Aegirine-
Augite
Jadeite
Aegirine
Jd
Ae
0.2
0.4
0.6
0.8
■ Sdh-1-ing
□ Sdh-1-Sym1
▲ Sdh-2-ing
△ Sdh-2-Sym1
b
$^{B}(Ca+\sum M^{2+})/\sum B \geq 0.75$, $^{B}Ca/\sum B \geq {}^{B}\sum M^{2+}/\sum B$
$^{A}(Na+K+2Ca)$ apfu
$^{C}(Al+Fe^{3+}+2Ti)$ apfu
0.0
0.5
1.0
1.5
2.0
Edenite
Pargasite
Sadanagaite
Tremolite
Magnesio-
hornblende
Tschermakite
● Sdh-1-ing
○ Sdh-1-Sym1
○ Sdh-1-Sym3
○ Sdh-1-rimg
■ Sdh-2-ing
□ Sdh-2-Sym1
□ Sdh-2-Sym3

Figure 6

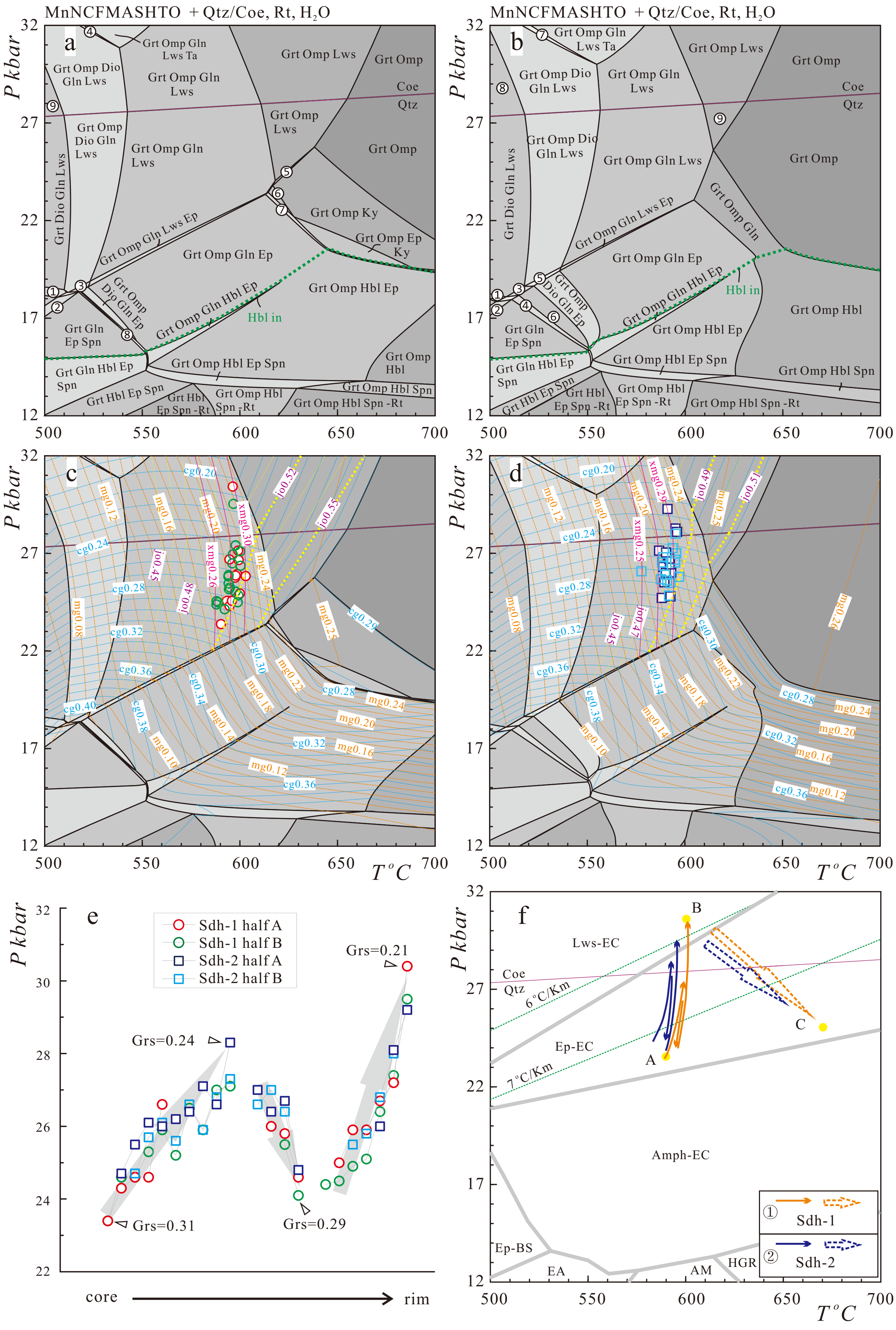
MnNCFMASHTO + Qtz/Coe, Rt, H_2O
a
b
c
d
e
f
P kbar
T °C
Grt Omp Gln Lws Ta
Grt Omp Dio Gln Lws
Grt Omp Gln Lws
Grt Omp Lws
Grt Omp
Coe
Qtz
Grt Omp Dio Gln Lws
Grt Dio Gln Lws
Grt Omp Gln Lws Ep
Grt Omp Gln Ep
Grt Omp Ky
Grt Omp Ep Ky
Grt Omp Hbl Ep
Hbl in
Grt Omp Dio Gln Ep
Grt Omp Gln Hbl Ep
Grt Gln Ep Spn
Grt Gln Hbl Ep Spn
Grt Omp Hbl Ep Spn
Grt Omp Hbl
Grt Omp Hbl Spn
Grt Hbl Ep Spn
Grt Hbl Ep Spn -Rt
Grt Omp Hbl Spn -Rt
Grt Omp Gln
Grt Omp Hbl Ep Spn
cg0.20
cg0.24
cg0.28
cg0.32
cg0.36
cg0.40
mg0.08
mg0.12
mg0.16
mg0.20
mg0.24
xmg0.26
xmg0.30
jo0.45
jo0.48
jo0.52
jo0.55
Sdh-1 half A
Sdh-1 half B
Sdh-2 half A
Sdh-2 half B
Grs=0.31
Grs=0.24
Grs=0.29
Grs=0.21
core
rim
Lws-EC
Ep-EC
Amph-EC
Ep-BS
EA
AM
HGR
6 °C/Km
7 °C/Km
A
B
C
① Sdh-1
② Sdh-2

Figure 7

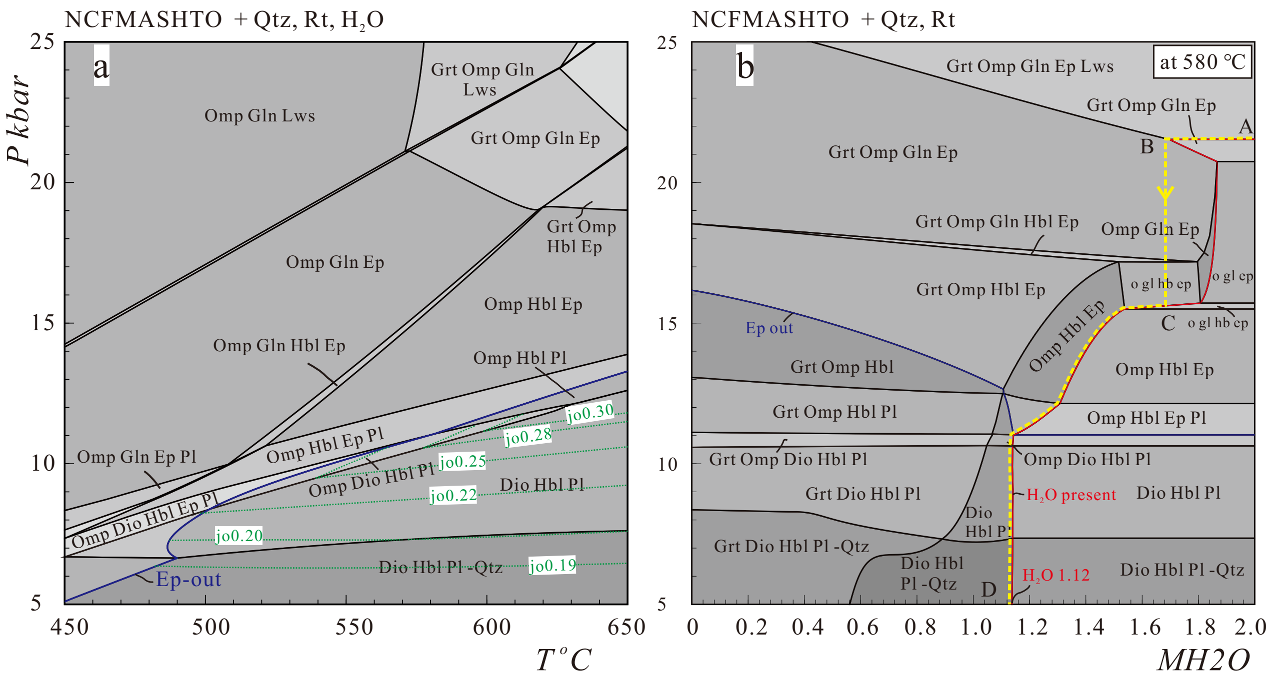
NCFMASHTO + Qtz, Rt, H₂O
a
P kbar
25
20
15
10
5
450
500
550
600
650
T °C
Omp Gln Lws
Grt Omp Gln Lws
Grt Omp Gln Ep
Omp Gln Ep
Grt Omp Hbl Ep
Omp Hbl Ep
Omp Gln Hbl Ep
Omp Hbl Pl
Omp Gln Ep Pl
Omp Hbl Ep Pl
Omp Dio Hbl Ep Pl
Omp Dio Hbl Pl
Dio Hbl Pl
Dio Hbl Pl -Qtz
Ep-out
jo0.30
jo0.28
jo0.25
jo0.22
jo0.20
jo0.19
NCFMASHTO + Qtz, Rt
b
at 580 ℃
0
0.2
0.4
0.6
0.8
1.0
1.2
1.4
1.6
1.8
2.0
MH2O
Grt Omp Gln Ep Lws
Grt Omp Gln Ep
A
B
C
D
Grt Omp Gln Ep
Grt Omp Gln Hbl Ep
Omp Gln Ep
o gl hb ep
o gl ep
Grt Omp Hbl Ep
Omp Hbl Ep
o gl hb ep
Ep out
Grt Omp Hbl
Omp Hbl Ep
Grt Omp Hbl Pl
Omp Hbl Ep Pl
Grt Omp Dio Hbl Pl
Omp Dio Hbl Pl
Grt Dio Hbl Pl
Dio Hbl Pl
H₂O present
Dio Hbl Pl
Grt Dio Hbl Pl -Qtz
Dio Hbl Pl -Qtz
H₂O 1.12
Dio Hbl Pl -Qtz

Figure 8

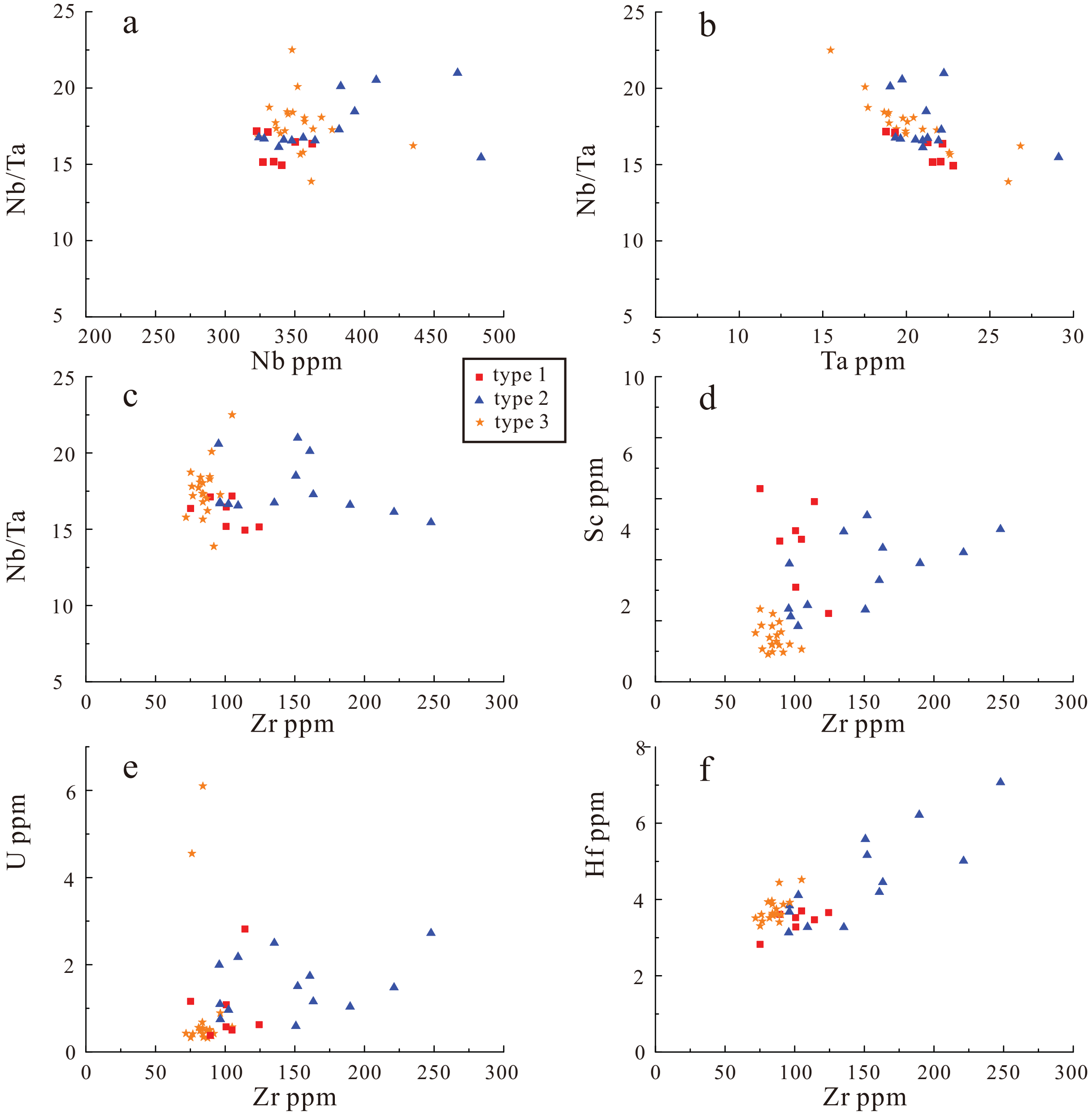
a
Nb/Ta
Nb ppm
b
Nb/Ta
Ta ppm
c
Nb/Ta
Zr ppm
type 1
type 2
type 3
d
Sc ppm
Zr ppm
e
U ppm
Zr ppm
f
Hf ppm
Zr ppm

Figure 9

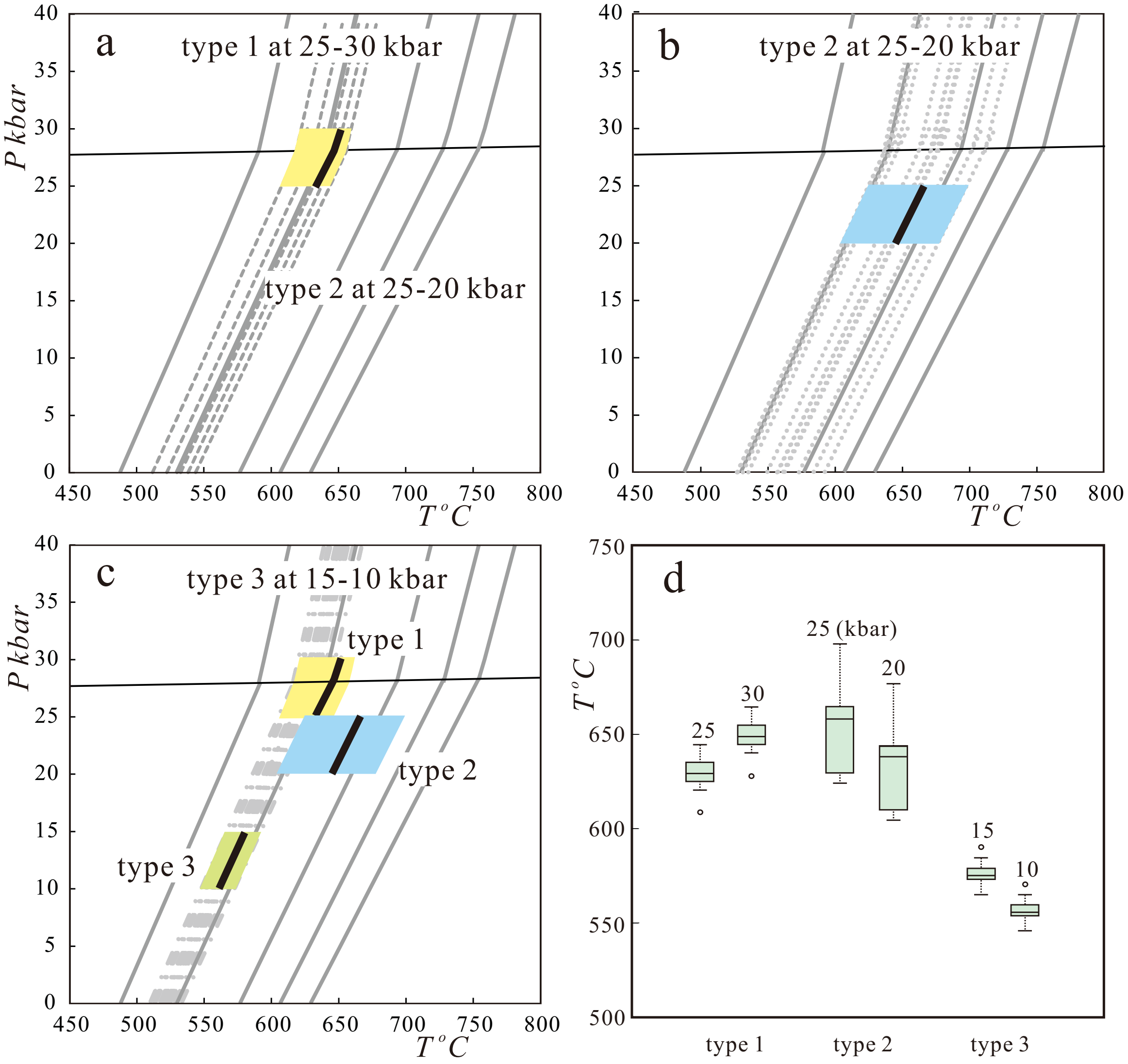
a
type 1 at 25-30 kbar
type 2 at 25-20 kbar
P kbar
T °C
b
type 2 at 25-20 kbar
c
type 3 at 15-10 kbar
type 1
type 2
type 3
d
T °C
25
30
25 (kbar)
20
15
10
type 1
type 2
type 3
0
5
10
15
20
25
30
35
40
450
500
550
600
650
700
750
800

Figure 10

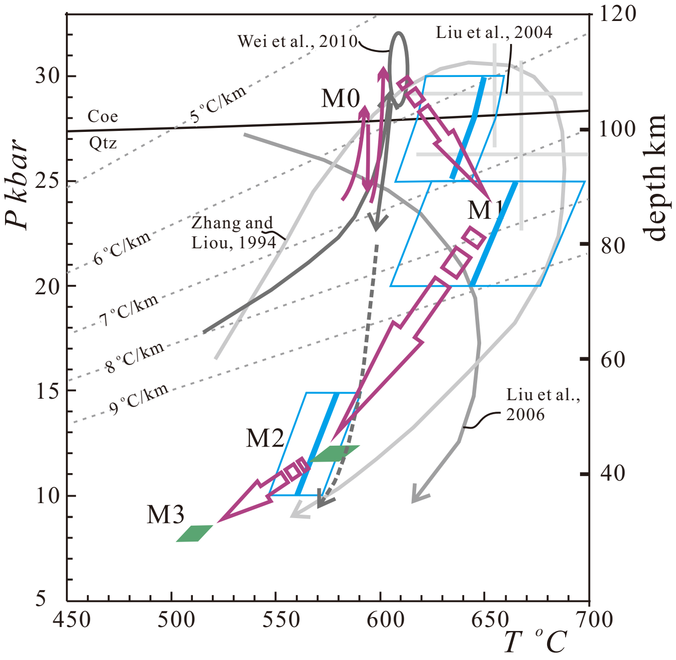
Wei et al., 2010
Liu et al., 2004
M0
M1
M2
M3
Coe
Qtz
5 °C/km
6 °C/km
7 °C/km
8 °C/km
9 °C/km
Zhang and Liou, 1994
Liu et al., 2006
P kbar
depth km
T °C
5
10
15
20
25
30
40
60
80
100
120
450
500
550
600
650
700

Figure 11